HIGH PERFORMANCE IMAGING USING ARRAYS OF INEXPENSIVE CAMERAS

A DISSERTATION
SUBMITTED TO THE DEPARTMENT OF ELECTRICAL ENGINEERING
AND THE COMMITTEE ON GRADUATE STUDIES
OF STANFORD UNIVERSITY
IN PARTIAL FULFILLMENT OF THE REQUIREMENTS
FOR THE DEGREE OF
DOCTOR OF PHILOSOPHY

Bennett Wilburn
December 2004

I certify that I have read this dissertation and that, in my opinion, it is fully adequate in scope and quality as a dissertation for the degree of Doctor of Philosophy.

Mark A. Horowitz Principal Adviser

I certify that I have read this dissertation and that, in my opinion, it is fully adequate in scope and quality as a dissertation for the degree of Doctor of Philosophy.

Pat Hanrahan

I certify that I have read this dissertation and that, in my opinion, it is fully adequate in scope and quality as a dissertation for the degree of Doctor of Philosophy.

Marc Levoy

Approved for the University Committee on Graduate Studies.

Abstract

Digital cameras are becoming increasingly cheap and ubiquitous, leading researchers to exploit multiple cameras and plentiful processing to create richer and more accurate representations of real settings. This thesis addresses issues of scale in large camera arrays. I present a scalable architecture that continuously streams color video from over 100 inexpensive cameras to disk using four PCs, creating a one gigasample-per-second photometer. It extends prior work in camera arrays by providing as much control over those samples as possible. For example, this system not only ensures that the cameras are frequency-locked, but also allows arbitrary, constant temporal phase shifts between cameras, allowing the application to control the temporal sampling. The flexible mounting system also supports many different configurations, from tightly packed to widely spaced cameras, so applications can specify camera placement. Even greater flexibility is provided by processing power at each camera, including an MPEG2 encoder for video compression, and FPGAs and embedded microcontrollers to perform low-level image processing for real-time applications.

I present three novel applications for the camera array that highlight strengths of the architecture and the advantages and feasibility of working with many inexpensive cameras: synthetic aperture videography, high speed videography, and spatiotemporal view interpolation. Synthetic aperture videography uses numerous moderately spaced cameras to emulate a single large-aperture one. Such a camera can see through partially occluding objects like foliage or crowds. I show the first synthetic aperture images and videos of dynamic events, including live video accelerated by image warps performed at each camera. High-speed videography uses densely packed cameras with staggered trigger times to increase the effective frame rate of the system. I show how to compensate for artifacts

induced by the electronic rolling shutter commonly used in inexpensive CMOS image sensors and present results streaming 1560 fps video using 52 cameras. Spatiotemporal view interpolation processes images from multiple video cameras to synthesize new views from times and positions not in the captured data. We simultaneously extend imaging performance along two axes by properly staggering the trigger times of many moderately spaced cameras, enabling a novel multiple-camera optical flow variant for spatiotemporal view interpolation.

Acknowledgements

In my early days as a graduate student, my peers warned me not to build a system as part of my thesis because it would add years to my stay here.

They were right.

Fortunately, these have been great years.

Designing, building, debugging, calibrating, and using an array of one hundred cameras is more work than one person can handle. I'd like to thank my friends and colleagues who helped get this show on the road: Monica Goyal, Kelin Lee, Alan Swithenbank, Eddy Talvala, Emilio Antunez, Guillaume Poncin, and Katherine Chou. Thanks also to the rest of the graphics crew who were so dang entertaining and also occasionally picked up a wrench to help rearrange scores of cameras: Augusto Roman, Billy Chen, and Gaurav Garg. Special thanks go to Michal Smulski, who was instrumental getting the early camera prototypes running. To Vaibhav Vaish, for all the calibration work, you da man. Finally, crazy props to Neel Joshi for his many contributions and for being there in crunch time.

My adviser, Mark Horowitz, has been a great inspiration. Mark, thanks for taking me on as a student, and thanks for being patient. I'm very grateful that you and my other readers, Marc Levoy and Pat Hanrahan, dreamed up this array project in the first place and gave me an opportunity to jump into vision and graphics. What a pleasant surprise that we never actually used the thing for light field rendering. Marc, your wild enthusiasm for one application after the next has been great motivation. Thanks also to Harry Shum for sending me back from China fired up to build these cameras and thinking about video compression.

SONY, Intel and Interval funded construction of the array through the Immersive Television Project. This work was also supported by DARPA grants F29601-00-2-0085 and

NBCH-1030009, and NSF grant IIS-0219856-001.

Of course, all work and no play... I'm not going to individually thank everyone who made my time here so meaningful and fun. You know who you are.

To Mom, Dad, Dadday, Lauri, Bob and Katherine: thanks for your love and support.

Contents

List of Tables

List of Figures

Chapter 1

Introduction

Digital cameras are becoming increasingly cheap and ubiquitous. In 2003, consumers bought 50 million digital still cameras and 84 million camera-equipped cell phones. These products have created a huge market for inexpensive image sensors, lenses and video compression electronics. In other electronics industries, commodity hardware components have created opportunities for performance gains. Examples include high-end computers built using many low-end microprocessors and clusters of inexpensive PCs used as web server or computer graphics render farms. The commoditization of video cameras prompts us to explore whether we can realize performance gains using many inexpensive cameras.

Many researchers have shown ways to use more images to increase the performance of an imaging system at a single viewpoint. Some combine pictures of a static scene taken from one camera with varying exposure times to create images with increased dynamic range [1, 2, 3]. Others stitch together pictures taken from one position with abutting fields of view to create very high resolution mosaics [4]. Another class of multi-image algorithms, view interpolation, uses samples from different viewpoints to generate images of a scene from new locations. Perhaps the most famous example of this technology is the Bullet Time special effects sequences in *The Matrix*. Extending most of these high-performance imaging and view interpolation methods to real, dynamic scenes requires multiple video cameras, and more cameras often yield better results.

Today one can easily build a modest camera array for the price of a high-performance studio camera, and it is likely that arrays of hundreds or even a thousand cameras will

soon reach price parity with these larger, more expensive units. Large camera arrays create new opportunities for high-performance imaging and view interpolation, but also present challenges. They generate immense amounts of data that must be captured or processed in real-time. For many applications, the way in which the data is collected is critical, and the cameras must allow flexibility and control over their placement, when they trigger, what range of intensities they capture, and so on. To combine the data from different cameras, one must calibrate them geometrically and radiometrically, and for large arrays to be practical, this calibration must be automatic.

Low-cost digital cameras present additional obstacles that must be overcome. Some are the results of engineering trade-offs, such as the color filter gels used in single-chip color image sensors. High-end digital cameras use three image sensor chips and expensive beam-splitting optics to measure red, green and blue values at each pixel. Cheaper, single-chip color image sensors use a pattern of filter gels over the pixels that subsamples color data. Each pixel measures only one color value–red, green or blue. The missing values at each pixel must be interpolated, from neighboring pixel data, which can cause errors. Other obstacles arise because inexpensive cameras take advantage of weaknesses in the human visual system. For example, because the human eye is sensitive to relative, not absolute, color differences, the color responses of image sensors are allowed to vary greatly from chip to chip. Many applications for large camera arrays will need to calibrate these inexpensive cameras to a higher precision than for their intended purposes.

1.1 Contributions

This thesis examines issues of scale for multi-camera systems and applications. I present the Stanford Multiple Camera Array, a scalable architecture that continuously streams color video from over 100 inexpensive cameras to disk using four PCs, creating a one gigasample-per-second photometer. It extends prior work in camera arrays by providing as much control over those samples as possible. For example, this system not only ensures that the cameras are frequency-locked, but also allows arbitrary, constant temporal phase shifts between cameras, allowing the application to control the temporal sampling. The flexible mounting system also supports many different configurations, from tightly

packed to widely spaced cameras, so applications can specify camera placement. As we will see, the range of applications implemented and anticipated for the array require a variety of physical camera configurations, including dense or sparse packing and overlapping or abutting fields of view. Even greater flexibility is provided by processing power at each camera, including an MPEG2 encoder for video compression, and FPGAs and embedded microprocessors to perform low-level image processing for real-time applications.

I also present three novel applications for the camera array that highlight strengths of the architecture and demonstrate the advantages and feasibility of working with large numbers of inexpensive cameras: synthetic aperture videography, high speed videography, and spatiotemporal view interpolation. Synthetic aperture videography uses many moderately spaced cameras to emulate a single large-aperture one. Such a camera can see through partially occluding objects like foliage or crowds. This idea was suggested by Levoy and Hanrahan [5] and refined by Isaksen et al. [6], but implemented only for static scenes or synthetic data due to lack of a suitable capture system. I show the first synthetic aperture images and videos of dynamic events, including live synthetic aperture video accelerated by image warps performed at each camera.

High-speed videography with a dense camera array takes advantage of the temporal precision of the array by staggering the trigger times of a densely packed cluster of cameras to create an effectively higher resolution video camera. Typically, high-speed cameras cannot stream their output continuously to disk and are limited to capture durations short enough to fit on volatile memory in the device. MPEG encoders in the array, on the other hand, compress the video in parallel, reducing the total data bandwidth and allowing continuous streaming to disk. One limitation of this approach is that the data from cameras with varying centers of projection must be registered and combined to create a single video. We minimize geometric alignment errors by packing the cameras as tightly as possible and choosing camera triggers orders that render artifacts less objectionable. Inexpensive CMOS image sensors commonly use an electronic rolling shutter, which is known to cause distortions for rapidly moving objects. I show how to compensate for these distortions by resampling the captured data and present results showing streaming 1560 fps video captured using 52 cameras.

The final application I present, spatiotemporal view interpolation, shows that we can

simultaneously improve multiple aspects of imaging performance. Spatiotemporal view interpolation is the generation of new views of a scene from a collection of input images. The new views are from places and times not in the original captured data. While previous efforts used cameras synchronized to trigger simultaneously, I show that using our array with moderately spaced cameras and staggered trigger times improves the spatiotemporal sampling resolution of our input data. Improved sampling enables simpler interpolation algorithms. I describe a novel, multiple-camera optical flow variant for spatiotemporal view interpolation. This algorithm is also exactly the registration necessary to remove the geometric artifacts in the high-speed video application caused by the cameras' varying centers of projection.

1.2 Contributions of Others to this Work

The Stanford Multiple Camera Array Project represents work done by a team of students. Several people made key contributions that are described in this thesis. The design of the array itself is entirely my own work, but many students aided in the implementation and applications. Michal Smulski, Hsiao-Heng Kelin Lee, Monica Goyal and Eddy Talvala each contributed portions of the FPGA Verilog code. Neel Joshi helped implement the high-speed videography and spatiotemporal view interpolation applications, and worked on several pieces of the system, including FPGA code and some of the larger laser-cut acrylic mounts. Guillaume Poncin wrote networked host PC software with a very nice graphical interface for the array, and Emilio Antunez improved it with support for real-time MPEG decoding.

Robust, automatic calibration is essential for large camera arrays, and two of my colleagues contributed greatly in this area. Vaibhav Vaish is responsible for the geometric calibration used by all of the applications in this thesis. His robust feature detector and calibration software is a major reason why the array can be quickly and accurately calibrated. The plane + parallax calibration method he devised and described in [7] is used for synthetic aperture videography and enabled the algorithm I devised for spatiotemporal view interpolation. Neel Joshi and I worked jointly on color calibration, but Neel did the

majority of the implementation. He also contributed many of the key insights, such as fixing the checker chart to our geometric calibration target and configuring camera gains by fitting the camera responses for gray scale Macbeth checkers to lines. Readers interested in more information are referred to Neel's Masters thesis [8].

1.3 Organization

The next chapter examines the performance and applications of past camera array designs and emphasizes the challenges of controlling and capturing data from large arrays. It reviews multiple image and multiple camera applications to motivate the construction of large camera arrays and set some of the performance goals they should meet. To scale economically, the Stanford Multiple Camera Array uses inexpensive image sensors and optics. Because these technologies might be expected to interfere with our vision and graphics applications, the chapter closes with a discussion of inexpensive sensing technologies and their implications for image quality and calibration.

Starting from the applications we intended to support and lessons learned from past designs, I set out to build a general-purpose research tool. Chapter 3 describes the Stanford Multiple Camera Array and the key technology choices that make it scale well. It summarizes the design, how it furthers the state of the art, and the particular features that enable the applications demonstrated in this thesis.

Chapters 4 through 6 present the applications mentioned earlier that show the value of the array and our ability to work effectively with many inexpensive sensors. Synthetic aperture photography requires accurate geometric image alignment but is relatively forgiving of color variations between cameras, so we present it and our geometric calibration methods first in chapter 4. Chapter 5 describes the high-speed videography method. Because this application requires accurate color-matching between cameras as well as good image alignment, I present our radiometric calibration pipeline here as well. Finally, chapter 6 describes spatiotemporal view interpolation using the array. This application shows not only that we can use our cameras to improve imaging performance along several metrics, but also that we can successfully apply computer vision algorithms to the data from our many cameras.

Chapter 2

Background

This chapter reviews previous work in multiple camera system design to better understand some of the critical capabilities of large arrays and how design decisions affect system performance. I also cover the space of image-based rendering and high-performance imaging applications that motivated construction of our array and placed additional demands on its design. For example, while some applications need very densely packed cameras, others depend on widely spaced cameras. Most applications require synchronized video, and nearly all applications must store all of the video from all of the cameras. Finally, because this work is predicated on cheap cameras, I conclude the chapter with a discussion of inexpensive image sensing and its implications for our intended applications.

2.1 Prior Work in Camera Array Design

2.1.1 Virtualized Reality

Virtualized Reality^{TM} [9] is the pioneering project in large video camera arrays and the existing setup most similar to the Stanford Multiple Camera Array. Their camera arrays were the first to capture data from large numbers of synchronized cameras. They use a model-based approach to view interpolation that deduces 3D scene structure from multiple views using disparity or silhouette information. Because they wanted to completely surround their working volume, they use many cameras spaced widely around a dome or

room.

The first iteration of their camera array design, called the 3D Dome, used consumer VCRs to record synchronized video from 51 monochrome CCD cameras [10, 9]. They routed a common sync signal from an external generator to all of their cameras. To make sure they could identify matching frames in time from different cameras, they inserted time codes from an external code generator into the vertical blanking intervals of each camera's video before it was recorded by the VCR. This system traded scalability for capacity. With one VCR per camera, they could record all of the video from all the cameras for essentially as long as they liked, but the resulting system is unwieldy and expensive. The quality of VCR video is also rather low, and the video tapes still had to be digitized, prompting an upgrade to digital capture and storage.

The next generation of their camera array, called the 3D-Room [11], captured very nice quality (640x480 pixel, 30fps progressive scan YCrCb) video from 49 synchronized color S-Video cameras. Their arrangement once again used external sync signal and time code generators to ensure frame accurate camera synchronization. To store all of the data in real-time, they had to use one PC for every three cameras. Large PC clusters are bulky and a challenge to maintain, and with very inexpensive cameras, the cost of the PCs can easily dominate the system cost. Even with the PC cluster, they were unable to fully solve the bandwidth problem. Because they stored data in each PC's 512MB main memory they were limited to nine second datasets and could not continuously stream. Even with these limitations, this was a very impressive system when it was first built six years ago.

2.1.2 Gantry-based Systems for Light Fields

The introduction of light fields by Levoy and Hanrahan [5], and Lumigraphs by Gortler et al. [12] motivated systems for capturing many images from very closely spaced viewing positions. Briefly, a light field is a two-dimensional array of (two-dimensional) images, hence a four-dimensional array of pixels. Each image is captured from a slightly different viewpoint. By assembling selected pixels from several images, new views can be constructed interactively, representing observer positions not present in the original array. If these views are presented on a head-tracked or autostereoscopic display, then the viewing

experience is equivalent to a hologram. These methods require very tightly spaced input views to prevent ghosting artifacts.

The earliest acquisition systems for light fields used a single moving camera. Levoy and Hanrahan used a camera on a mechanical gantry to capture the light fields of real objects in [5]. They have since constructed a spherical gantry [13] for capturing inward-looking light fields. Gantries have the advantage of providing unlimited numbers of input images, but even at a few seconds per image, it can take several hours to capture a full light field. Gantries also require very precise motion control, which is expensive. The biggest drawback, of course, is that they cannot capture light fields of dynamic scenes. Capturing video light fields, or even a single light field "snapshot" of a moving scene, requires a camera array.

2.1.3 Film-Based Linear Camera Arrays

Dayton Taylor created a modular, linear array of linked 35mm cameras to capture dynamic events from multiple closely spaced viewpoints at the same time [14]. A common strip of film traveled a light-tight path through all of the adjacent cameras. Taylor's goal was to decouple the sense of time progressing due to subject motion and camera motion. Because his cameras were so closely spaced he could create very compelling visual effects of virtual camera motion through "frozen" scenes by hopping from one view to the next. His was the first system to introduce these effects into popular culture.

2.1.4 Bullet Time

Manex Entertainment won the 2002 Academy Award ® for Best Achievement in Visual Effects for their work in *The Matrix*. The trademark shots in that film were the "Bullet Time" sequences in which moving scenes were slowed to a near standstill while the camera appeared to zoom around them at speeds that would be impossible in real life. Their capture system used two cameras joined by a chain of over 100 still cameras and improved upon Taylor's in two ways. The cameras were physically independent from each other and could be spaced more widely apart to cover larger areas, they could be sequentially triggered with very precise delays between cameras. After aligning the still images, the actors

were segmented from them and placed in a computer-generated environment that moved in accordance with the apparent camera motion.

Like Taylor's device, this camera array is very special-purpose, but it is noteworthy because the sequences produced with it have probably exposed more people to image-based rendering techniques than any others. They show the feasibility of combining data from many cameras to produce remarkable effects. The system is also the first I know of with truly flexible timing control. The cameras were not just synchronized—they could be triggered sequentially with precisely controlled delays between each camera's exposure. This gave Manex unprecedented control over the timing of their cameras.

2.1.5 Dynamic Light Field Viewer

Yang et al. aimed at a different corner of the multiple camera array space with their real-time distributed light field camera [15]. Their goal was to create an array for rendering a small number of views from a light field acquired in real-time with a tightly packed 8x8 grid of cameras. One innovative aspect of their design is that rather than using relatively expensive cameras like the 3D Room, they opted for inexpensive commodity webcams. This bodes well for the future scalability of their system, but the particular cameras they chose had some drawbacks. The quality was rather low at 320x240 pixels and 15fps. The cameras had no clock or synchronization inputs, so their acquired video was synchronized only to within a frame time. Especially at 15fps, the frame to frame motion can be quite large for dynamic scenes, causing artifacts in images rendered from unsynchronized cameras. Unsynchronized cameras also rule out multiple view depth algorithms that assume rigid scenes.

A much more limiting choice they made was not to store all of the data from each camera. This, along with the lower camera frame rate and resolution, was their solution to the bandwidth challenge. Instead of capturing all of the data, they implemented what they call a "finite-view" design, meaning the system returns from each camera only the data necessary to render some small finite number of views from the light field. As they point out, this implies that the light field cannot be stored for later viewing or used to drive a hypothetical autostereoscopic display. Moreover, although they did not claim that

had any goals for their hardware other than the light field viewing, the finite-view design means that their device is essentially single-purpose. It cannot be used for applications that require video from all cameras. Thus, the bandwidth problem was circumvented at the cost of flexibility and quality.

2.1.6 Self-Reconfigurable Camera Array

The Self-Reconfigurable Camera Array developed by Zhang and Chen has 48 cameras with electronically controlled pan and horizontal motion [16]. The aim of their project is to improve view interpolation by changing the camera positions and orientations in response to the scene geometry and the desired virtual viewpoint. Although electronically controlled camera motion is an interesting property, they observe that their system performance was limited by decisions to use commodity ethernet cameras and a single PC to run the array. The bandwidth constraints of their ethernet bus limit them to low quality, 320x240 images. They also note that because they cannot easily synchronize their commodity cameras, their algorithms for reconfiguring the array do not track fast objects well.

2.2 View Interpolation and High-X Imaging

All of the arrays mentioned in the previous section were used for view interpolation, and as such are designed for each camera or view to capture a unique perspective image of a scene. This case is called *multiple-center-of-projection (MCOP)* imaging [17]. If instead the cameras are packed closely together, and the scene is sufficiently far away or shallow, then the views provided by each camera are nearly identical or can be made so by a projective warp. We call this case *single-center-of-projection (SCOP)* imaging. In this mode, the cameras can operate as a single, synthetic “high-X” camera, where X can be resolution, signal-to-noise ratio, dynamic range, depth of field, frame rate, spectral sensitivity, and so on. This section surveys past work in view interpolation and high-X imaging to determine the demands they place on a camera array design. As we will see, these include flexibility in the physical configuration of the cameras, including very tight packing; precise control over the camera gains, exposure durations, and trigger times; and synchronous capture.

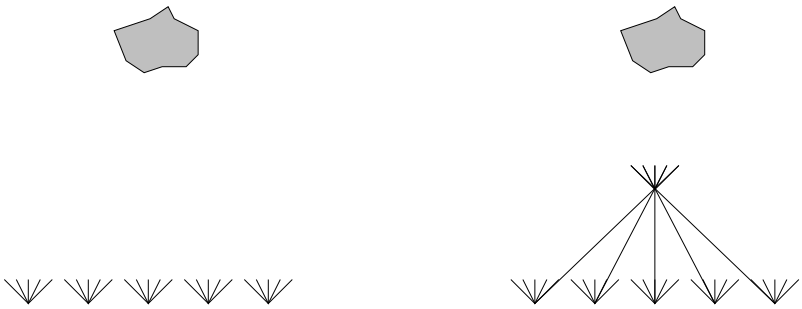

(a) Acquiring a light field using an array of cameras.

(b) Rendering new views from a light field.

Figure 2.1: Light Field Rendering uses arrays of images to create new views of a scene. (a) Sampling the light field using an array of cameras. (b) Rendering a new view. Each ray in the new view is mapped to rays from the acquired images. In this simplified diagram, the rays can be mapped exactly to rays from the cameras. Generally, the exact ray from the virtual viewpoint is not captured by any one camera, so it is interpolated from the nearest sampled rays.

2.2.1 View Interpolation

View interpolation algorithms use a set of captured images of a scene to generate views of that scene from new viewpoints. These methods can be categorized by the trade-off between the number of input images and the complexity of the interpolation process. The original inspiration for the Stanford Multiple Camera Array, Levoy and Hanrahan's work on Light Field Rendering [5], lies at the extreme of using very large numbers of images and very simple interpolation. The light field is the radiance as a function of position and direction in free (unoccluded) space. Using a set of cameras, one can sample the light field on a surface in space. To create a new view, one simply resamples the image data. Figure 2.1 shows this in two dimensions.

Light field rendering is an example of image-based rendering (IBR). Traditional model-based renderers approximate physics using models of the illumination, three-dimensional structure and surface reflectance properties of a scene. Model-based rendering can produce very compelling results, but the complexity of the models and rendering grows with the

complexity of the scene, and accurately modeling real scenes can be very difficult. Image-based rendering, on the other hand, uses real or pre-rendered images to circumvent many of these challenges. Chen and Williams used a set of views with precomputed correspondence maps to quickly render novel views using image morphs [18]. Their method has a rendering time independent of scene complexity but requires a correspondence map and has trouble filling holes when occluded parts of the scene become visible.

Light field rendering uses no correspondence maps or explicit 3D scene models. As described earlier, new views are generated by combining and resampling the input images. Although rendering light fields is relatively simple, acquiring them can be very challenging. Light fields typically use over a thousand input images. The original light field work required over four hours to capture a light field of a static scene using a single translating camera. For dynamic scenes, one must use a camera array–the scene will not hold still while a camera is translated to each view position. Light field rendering requires many very closely spaced images to prevent aliasing artifacts in the interpolated views. Ideally the camera spacing would be equal to the aperture size of each camera, but practically, this is impossible. Dynamic scenes require not only multiple cameras, but also methods to reduce the number of required input views.

The Virtualized Reality [9] work of Rander et al. uses fewer images at the expense of increasing rendering complexity. They surround their viewing volume with cameras and then infer the three-dimensional structure of the scene using disparity estimation or voxel carving methods [19, 20]. Essentially, they are combining model-based and image-based rendering. They infer a model for the scene geometry, but compute colors by resampling the images based on the geometric model. Matusik et al. presented another view interpolation method, Image Based Visual Hulls [21], that uses silhouettes from multiple views to generate approximate structural models of foreground objects. Although these methods use fewer, more widely separated cameras than Light Field Rendering, inferring structure using multiple cameras is still an unsolved vision problem and leads to artifacts in the generated views.

How should a video camera array be designed to allow experiments across this range of view interpolation methods? At the very least, it should store all of the data from all cameras for reasonable length videos. At video rates (30fps), scene motion, and hence the

image motion from frame to frame, can be quite significant. Most methods for inferring 3D scene structure assume a rigid scene. For an array of video cameras, this condition will only hold if the cameras are synchronized to expose at the same time. For pure image-based methods like Light Field Rendering, unsynchronized cameras will result in ghost images. Light Field Rendering requires many tightly packed cameras, but Virtualized Reality and Image Based Visual Hulls use more widely separated cameras, so clearly a flexible camera array should support both configurations. Finally, all of these applications assume that the cameras can be calibrated geometrically and radiometrically.

2.2.2 High-X Imaging

High-X imaging combines many single-center-of-projection images to extend imaging performance. To shed light on camera array design requirements for this space, I will now enumerate several possible high-X dimensions, discuss prior work in these areas and consider how we might implement some of them using a large array of cameras.

High-X Imaging Dimensions

High Resolution. Images taken from a single camera rotating about its optical center can be combined to create high-resolution, wide field-of-view (FOV) panoramic image mosaics [4]. For dynamic scenes, we must capture all of the data simultaneously. Imaging Solutions Group of New York, Inc, offers a "quad HDTV" 30 frame-per-second video camera with a 3840 x 2160 pixel image sensor. At 8.3 megapixels per image, this is the highest resolution video camera available. This resolution could be surpassed with a 6 x 5 array of VGA (640 x 480 pixel) cameras with abutting fields of view. Many companies and researchers have already devised multi-camera systems for generating video mosaics of dynamic scenes [22]. Most pack the cameras as closely together as possible to approximate a SCOP system, but some use optical systems to ensure that the camera centers of projection are actually coincident. As the number of cameras grow, these optical systems become less practical.

If the goal is just wide field of view or panoramic imaging, but not necessarily high resolution, then a single camera can be sufficient. For example, the Omnicamera created by Nayar uses a parabolic mirror to image a hemispherical field of view [23]. Two such

cameras placed back-to-back form an omnidirectional camera.

Low Noise. It is well known that averaging many images of the same scene reduces image noise (measured by the standard deviation from the expected value) by the square root of the number of images, assuming the noise is zero-mean and uncorrelated between images. Using an array of 100 cameras in SCOP mode, we should be able to reduce image noise by a factor of 10.

Super-Resolution. It is possible to generate a higher resolution image from a set of displaced low-resolution images if one can measure the camera's point spread function and register the low-resolution images to sub-pixel accuracy [24]. We could attempt this with an array of cameras. Unfortunately, super-resolution is fundamentally limited to less than a two-fold increase in resolution, and the benefits of more input images drops off rapidly [25, 26], so abutting fields of view is generally a better solution for increasing image resolution. On the other hand, many of the high-X methods listed here use cameras with completely overlapping fields of view, and we should be able to achieve a modest resolution gain with these methods.

Multi-Resolution Video. Multi-resolution video allows high-resolution (spatially or temporally) insets within a larger lower-resolution video [27]. Using an array of cameras with varying fields of view, we could image a dynamic scene at multiple resolutions. One use of this would be to provide high-resolution foveal insets within a low-resolution panorama. Another would be to circumvent the limits of traditional super-resolution. Information from high-resolution images can be used to increase resolution of a similar low-resolution image using texture synthesis [28], image alignment [29], or recognition-based priors [26]. In our case, we would use cameras with narrower fields of view to capture representative portions of the scene in higher resolution. Another version of this would be to combine a high-speed, low-resolution video with a low-speed, high-resolution video (both captured using high-X techniques) to create a single video with higher frame rate and resolution.

High Dynamic Range. Natural scenes often have dynamic ranges (the ratio of brightest to darkest intensity values) that far exceed the dynamic range of photographic negative film or the image sensors in consumer digital cameras. Areas of a scene that are too bright saturate the film or sensor and look uniformly white, with no detail. Regions that are too dark can be either be drowned out by noise in the sensor or simply not detected due to the sensitivity limit of the camera. Any given exposure only captures a portion of the total dynamic range of the scene. Mann and Picard [2], and Debevec and Malik [3] show ways to combine multiple images of a still scene taken with different known exposure settings into one high dynamic range image. Using an array of cameras with varying aperture settings, exposure durations, or neutral density filters, we could extend this idea to dynamic scenes.

High Spectral Sensitivity. Humans have trichromatic vision, meaning that any incident light can be visually matched using combinations of just three fixed lights with different spectral power distributions. This is why color cameras measure three values, roughly corresponding to red, green and blue. Multi-spectral images sample the visible spectrum more finely. Schechner and Nayar attached a spatially varying spectral filter to a rotating monochrome camera to create multi-spectral mosaics of still scenes. As they rotate their camera about its center of projection, points in the scene are imaged through different regions of the filter, corresponding to different portions of the visible spectrum. After registering their sequence of images, they create images with much finer spectral resolution than the three typical RGB bands. Using an array of cameras with different band-pass spectral filters, we could create multi-spectral videos of dynamic scenes.

High Depth of Field. Conventional optical systems can only focus well on objects within a limited range of depths. This range is called the depth of field of the cameras, and it is determined primarily by the distance at which the camera is focused (depth of field increases with distance) and the diameter of the camera aperture (larger apertures result in a smaller depth of field). For static scenes, depth of field can be extended using several images with different focal depths and selecting, for each pixel, the value from the image in which is is best focused [30]. The same principle could be applied to a SCOP camera array. One challenge is that depth of field is most limited close to the camera, where the

SCOP approximation for a camera array breaks down. Successfully applying this method would require either an optical system that ensures a common center of projection for the cameras or sophisticated image alignment algorithms.

Large Aperture. In chapter 4, I describe how we use our camera array as a large synthetic aperture camera. I have already noted that the very narrow depth of field caused by large camera apertures can be exploited to look beyond partially occluding foreground objects, blurring them so as to make them invisible. In low-light conditions, large apertures are also useful because they admit more light, increasing the signal-to-noise ratio of the imaging system. This is the one high-X application that is deliberately not single-center-of-projection. Instead, it relies on slightly different centers of projection for all cameras.

High Speed. Typical commercial high-speed cameras run at frame rates of hundreds to thousands of frames per second, and high-speed video cameras have been demonstrated running as high as one million frames per second [31]. As frame rates increase for a fixed resolution, continuous streaming becomes impossible, limiting users to short recording durations. Chapter 5 discusses in detail high-speed video capture using the Stanford Multiple Camera Array. Here, I will just reiterate that we use many sensors with evenly staggered triggers, and that parallel capture (and compression) permits continuous streaming.

Camera Array Design for High-X Imaging

A camera array for High-X imaging should allow all of the fine control over various camera parameters required by traditional single-camera applications but also address the issues that arise when those methods are extended to multiple cameras. For multiple-camera high-x applications, the input images should generally be views of the same scene at the same time from the same position, from cameras that respond identically to and capture the same range of intensities. Thus, the cameras should be designed to be tightly packed to approximate a single center of projection, synchronized to trigger simultaneously, and configured with wholly overlapping fields of view. Furthermore, we must set their exposure times and color gains and offsets to capture the same range of intensities. None of these

steps can be done perfectly, and the cameras will always vary, so we will need to calibrate geometrically and radiometrically to correct residual errors.

For most high-x applications, at least one parameter must be allowed to vary, so a camera array should also support as much flexibility and control over as many camera properties as possible. In fact, we find reason to break every guideline listed above. For example, to capture high dynamic range images, we configure the cameras to sense varying intensity ranges. Synthetic aperture photography explicitly defies the SCOP model to capture multiple viewpoints. To use the array for high-resolution capture, we must abut the fields of view instead of overlapping them. Finally, high-speed imaging relies on precisely staggered, not simultaneous, trigger times. Flexibility is essential.

2.3 Inexpensive Image Sensing

Nearly all of the applications and arrays presented so far used relatively high quality cameras. How will these applications map to arrays of inexpensive image sensors? Cheap image sensors are optimized to produce pictures to be viewed by humans, not by computers. This section discusses how cheap sensors exploit our perceptual insensitivity to certain types of imaging errors and the implications of these optimizations for high performance imaging.

2.3.1 Varying Color Responses

The vast majority of image sensors are used in single-camera applications where the goal is to produce pleasing pictures, and human color perception senses relative differences between colors, not absolute colors [32]. For these reasons, manufacturers of image sensors are primarily concerned with only the relative accuracy of their sensors. Auto-gain and auto-exposure ensure the image is exposed properly, and white balancing algorithms adjust color gains and the output image to fit some assumption of the color content of the scene. These feedback loops automatically compensate for any variations in the sensor response while they account for external factors like the illumination. Without a reference, it is often difficult for us to judge the fidelity of the color reproduction.

For IBR and high-X applications that use just one camera to capture multiple images, the actual shape of the sensor's response curve (i.e. digital pixel value as a function of incident illumination), and its response to light of different wavelengths, are unimportant as long as they are constant and the response is monotonic. With multiple cameras, differences in the absolute response of each camera become relative differences between their images. These differences can be disastrous if the images are directly compared, either by a human or an algorithm. A panoramic mosaic stitched together from cameras with different responses will have an obviously incorrect appearance, even if each region viewed individually looks acceptable. Methods that try to establish corresponding scene points in two images often assume brightness constancy, meaning that a scene point appears the same in all images of it. Correcting the color differences between cameras is essential for these applications.

Because so few end users care about color matching between sensors, variations in color response between image sensors are poorly documented. In practice, these differences can be quite large. In chapter 5, I will show that for the image sensors in the array, the color responses of 100 chips set to the same default gain and exposure values varies quite widely.

2.3.2 Color Imaging and Color Filter Arrays

One key result of color science is that because the human eye has only three different types of cones for detecting color, it is possible to represent all perceptually discernible colors with just three primaries, each having linearly independent spectral power distributions. Practically, this means that color image sensors only need to measure the incident illumination using detectors with three appropriately chosen spectral responses instead of measuring the entire spectra. Typically, these responses correspond roughly to what we perceive as red, green and blue. Each pixel in an image sensor makes only one measurement, so some method must be devised to measure three color components.

High-end color digital cameras commonly use three image sensors and special optics that send the incident red light to one sensor, the green to another, and the blue to a third. This measures three color values at each pixel, but the extra image sensors and precisely aligned optics increase the total cost of camera.

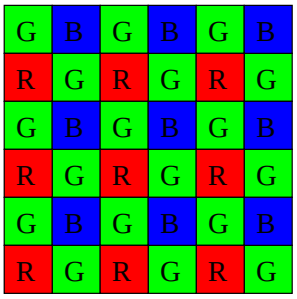

Figure 2.2: The Bayer Mosaic color filter array. Each pixel senses only one of red, green or blue. Missing color values must be interpolated from neighboring pixels.

Inexpensive, single-chip color cameras use one image sensor with a color filter array on top of the pixels. Instead of measuring red, green and blue values at each pixel, they measure red, green *or* blue. One example filter array pattern, the Bayer Mosaic [33], is shown in figure 2.2. The pattern exploits two properties of human visual perception: we are more sensitive to high frequency luminance information than chrominance, and our perception of intensity depends most heavily on green light. Every other pixel has a green filter, and the remaining two quarters are split between red and blue. Compared to the three-chip solution, two thirds of the color information is lost at each pixel.

Mosaic images must be "demosaiced", or interpolated, to generate a three-color RGB values at each pixel. Naive methods to interpolate the missing color values, like simple nearest neighbor replication or bilinear interpolation, can cause severe aliasing and false colors near intensity edges. Adaptive algorithms [34, 35] perform better at edges, but because the problem is ill-posed, no method will always be free of artifacts. These artifacts can be both visually objectionable and troubling for vision algorithms.

2.3.3 Inexpensive Manufacturing Methods

Manufacturing processes for cheap cameras are less precise than for expensive cameras. Wider variations in device performance are tolerated in order to increase yields, meaning that image quality will suffer. For example, noisier image sensors may not be culled during production, and wider color variations will be tolerated, as mentioned previously. As we will see in later sections on camera calibration, standard camera models assume an image

plane that is perpendicular to the lens' optical axis. On inexpensive sensors, however, the dies may be tilted and rotated on the package, violating that model.

The optical systems for cheap cameras are also of lower quality. Although glass lenses produce better images, very cheap cameras use plastic lenses or hybrid glass-plastic lenses instead. Furthermore, avoiding artifacts such as spherical and chromatic aberration requires multiple lens elements, which will be less precisely placed in a cheap sensor. Less precise placement will cause distortions in the image and more inconsistencies between the camera and commonly used models. Finally, high-quality lenses provide adjustments to control the aperture size and focal length, but in inexpensive lenses, these quantities are fixed.

In the next chapter, I describe the Stanford Multiple Camera Array and the design decisions I made in its implementation. One goal for the system was to use cheaper, lower-quality components and compensate for their drawbacks in software where possible. Thus, we chose fixed-focus, fixed-aperture lenses for their affordability. Similarly, the decreased cost and complexity of designing single-chip color cameras outweighed the disadvantages of subsampled color due to the Bayer Mosaic. These are two examples of the many trade-offs involved in the design of the array.

Chapter 3

The Stanford Multiple Camera Array

The broad range of applications for camera arrays combined with the promise of inexpensive, easy to use, smart cameras and plentiful processing motivated exploration of the potential of large arrays of cheap cameras. In this chapter, I present a scalable, general-purpose camera array that captures video continuously from over 100 precisely-timed cameras to just four PCs. Instead of using off-the-shelf cameras, I designed custom ones, leveraging existing technologies for our particular goals. I chose CMOS image sensors with purely digital interfaces so I could easily control the gain, exposure and timing for all the cameras. MPEG2 video compression at each camera reduces the data bandwidth of the system by an order of magnitude. High-speed IEEE1394 interfaces make the system modular and easily scalable. Later chapters show the array being used in a variety of configurations for several different applications. Here, I explain the technology that makes this possible.

3.1 Goals and Specifications

The Stanford Multiple Camera Array is intended to be a flexible research tool for exploring applications of large numbers of cameras. At the very least, I wanted to be able to implement IBR and High-X methods similar to those described in the previous chapter. This requires large numbers of cameras with precise timing control, the ability to tightly pack or widely space the cameras, and low-level control over the camera parameters. For the device to be as general as possible, it should capture and store all data from all the cameras. I

also wanted the architecture to be modular and easily scalable so it could span applications requiring anywhere from a handful to over one hundred cameras. One implication of this scalability was that even though the array might have over one hundred cameras, it should use far fewer than one hundred PCs to run it, ideally just a handful. Finally, reconfiguring the array for different applications should not be a significant obstacle to testing out new ideas.

To begin quantifying the specifications of our array, I started with the same video resolution and frame rate as the 3D Room: 640x480 pixel, 30fps progressive scan video. 30fps is generally regarded as the minimum frame rate for real-time video, and 640x480 is suitable for full-screen video. To demonstrate scalability, I aimed for a total of 128 cameras. To record entire performances, I set a goal of recording video sequences at least ten minutes long.

No off-the-shelf solution could meet these design goals. The cameras had to be tiny and provide a means to synchronize to each other. I also wanted to be able to control and stream video from at least 30 of the cameras to a single PC. There simply were no cameras on the market that satisfied these needs. By building custom cameras, I was able to explicitly add the features I needed and leave room to expand the abilities of the cameras in the future.

3.2 Design Overview

The Stanford Multiple Camera array streams video from many CMOS image sensors over IEEE1394 buses to a small number of PCs. Pixel data from each sensor flows to an FPGA that routes it to local DRAM memory for storage or to an IEEE1394 chipset for transmission to a PC. The FPGA can optionally perform low-level image processing or pass the data through an MPEG encoder before sending it to the 1394 chipset. An embedded microprocessor manages the components in the camera and communicates with the host PCs over IEEE1394. In this section, I describe the major technologies used in the array: CMOS image sensors, MPEG video compression, and IEEE1394 communication.

3.2.1 CMOS Image Sensors

One of the earliest decisions for the array was to use CMOS instead of CCD image sensors. CCDs are fully analog devices, requiring more careful design, supporting electronics to digitize their output, and often multiple supply voltages or clocks. CMOS image sensors, on the other hand, generally run off standard logic power supplies, can output 8-or 16 bit-digital video, and can connect directly to other logic chips. Sensor gains, offsets, exposure time, gamma curves and more can often be programmed into registers on the chip using standard serial interfaces. Some CMOS sensors even have digital horizontal and vertical sync inputs for synchronization. These digital interfaces make the design simpler and more powerful. Immediate practical concerns aside, because digital logic can be integrated on the same chip, CMOS sensors offer the potential of evolving into "smart" cameras, and it seemed sensible to base our design on that technology.

The many advantages of using CMOS sensors come with a price. CMOS sensors are inherently noisier [36] and less sensitive than their CCD counterparts. For these reasons, CCD sensors are still the technology of choice for most high performance applications [37]. I decided to sacrifice potential gains in image quality in exchange for a much more tractable design and added functionality.

3.2.2 MPEG2 Video Compression

The main goals for the array are somewhat contradictory: it should store all of the video from all of our cameras for entire performances, but also scale easily to over one hundred cameras using just a handful of PCs. An array of 128, 640x480 pixel, 30fps, one byte per pixel, Bayer Mosaic video cameras generates over 1GB/sec of raw data, roughly twenty times the maximum sustained throughput for today's commodity hard drives and peripheral interfaces. The creators of the 3D Room attacked this problem by storing raw video from cameras to main memory in PCs. With 49 cameras and 17 PCs with 512MB of main memory, they were able to store nearly 9 seconds of video. To capture much longer datasets using far fewer PCs, I took a different approach: compressing the video.

One video compression option for the array was DCT-based intra-frame video encoding

like DV. Commercial DV compression hardware was either too costly are simply unavailable when I built the array. MPEG2 uses motion prediction to encode video with a much higher compression ratio, and Sony, one of the early sponsors of this work, offered their MPEG2 compression chips at a reasonable price. A relatively standard 5Mb/s bitstream for 640x480, 30fps video translates into a compression ratio of 14:1, and at 4Mb/s, the default for the Sony encoder, this results in 17.5:1 compression. 128 cameras producing 5Mb/s bitstreams create 80MB/s of data, back in the ballpark of bandwidths we might hope to get from standard peripheral buses and striped hard drives. The disadvantage of MPEG compression is that it is lossy, meaning that one cannot exactly reproduce the original uncompressed video. I opted to use it anyway, but in order to investigate the effects of compression artifacts I designed the cameras to simultaneously store brief segments of raw video to local memory while streaming compressed video. This lets one compare MPEG2 compressed video with raw video for array applications.

3.2.3 IEEE1394

The last piece of the array design was a high bandwidth, flexible and scalable means to connect cameras to the host PCs. I chose the IEEE1394 High Performance Serial Bus [38], which has several properties that make it ideal for this purpose. It guarantees a default bandwidth of 40MB/s for "isochronous" transfers, data that is sent at a constant rate. This is perfect for streaming video, and indeed many digital video cameras connect to PCs via IEEE1394 (also known as FireWire® and i-Link®). IEEE1394 is also well suited for a modular, scalable design because it allows up to 63 devices on each bus and supports plug and play. As long as the bandwidth limit for a given bus is not exceeded, one can add or remove cameras at will and the bus will automatically detect and enumerate each device. Another benefit of IEEE1394 is the cabling environment. IEEE1394 cables can be up to 4.5m long, and an entire bus can span over 250m, good news if we want to space our cameras very widely apart, say on the side of a building.

The combination of MPEG2 and IEEE1394 creates a natural "sweet spot" for a large camera array design. A full bus can hold 63 devices; if we set aside one device for a host PC, it can still support up to 62 cameras. 62 MPEG2 video streams at 5Mb/s add

up to 310Mb/s of data, just within the default 320Mb/s limit of the bus. 320Mb/s is also well within the bandwidth of two software striped IDE hard drives, so this setup means I could reasonably hope to require only one PC per 60 cameras in our architecture. For reasons I will discuss later, the current system supports only 25 cameras per PC with 4Mb/s bitstreams, but a more sophisticated implementation should be able to approach a full set of 62 cameras per bus.

3.3 System Architecture

To be scalable and flexible, the system architecture had to not only meet the video capture requirements but also easily support changes in the number of cameras, their functionality, and their placement. Each camera is a separate IEEE1394 device, so adding or removing cameras is simple. I embedded a microprocessor to manage the IEEE1394 interface, the image sensor and the MPEG encoder. Accompanying the processor is an EEPROM for a simple boot loader and DRAM memory for storing image data and an executable downloaded over the IEEE1394 bus. The image sensor, MPEG encoder and IEEE1394 chips all have different data interfaces, so I added an FPGA for glue logic. Anticipating that I might want to add low-level image processing to each camera, I used a higher-performance FPGA than necessary and connected it to extra SRAM and SDRAM memory. Because the timing requirements for the array were stricter than could be achieved using IEEE1394 communication, especially with multiple PCs, I added CAT5 cables to each camera to receive the clock and trigger signals and propagate them to two other nodes. All of these chips and connections take up more board area than would fit on a tiny, densely-packable camera, so I divided the cameras into two pieces: tiny camera “tiles” containing just the image sensor and optics, and larger boards with the rest of the electronics.

Figure 3.1 shows how the cameras are connected to each other and to the host PCs using a binary tree topology. One camera board is designated as the root camera. It generates clocks and triggers that are propagated to all of the other cameras in the array. The root is connected via IEEE1394 to the host PC and two children. The CAT5 cables mirror the IEEE1394 connections between the root camera and the rest of the array. When camera numbers or bandwidth exceed the maximum for one IEEE1394 bus, we use multiple buses,

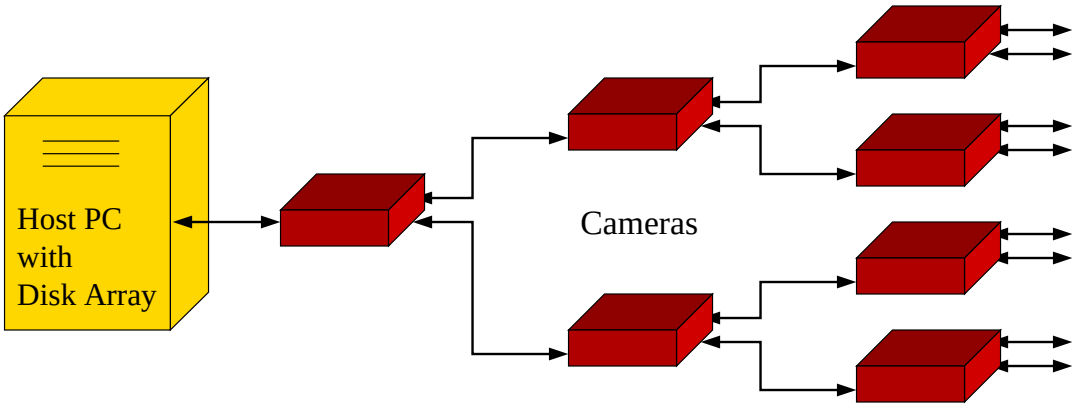

Figure 3.1: Camera array architecture

each connected to their own host PC. In this case, only one bus holds the root camera, and the clock and trigger signals are routed from it to the entire array.

3.3.1 Camera Tiles

For the camera tile, I looked for a digital, color, 640x480 pixel, 30fps image sensor with synchronization inputs. The SONY MPEG encoder requires YUV422 format input, but for research purposes, I also wanted access to the raw RGB Bayer data. The Omnivision OV8610 was the only sensor that met these needs. The OV8610 provides 800x600 pixel, 30fps progressive scan video. Our MPEG encoder can handle at most 720x480 pixel video, but currently we use only 640x480, cropped from the center of the OV8610 image. The OV8610 has a two-wire serial interface for programming a host of registers controlling exposure times, color gains, gamma, video format, region of interest, and more.

Early on, I considered putting multiple sensors onto one printed circuit board to allow very tight packing and to fix the cameras relative to each other. I had hoped that the rigid positioning of the cameras would make them less likely to move relative to each other after geometric calibration. I constructed a prototype to test this arrangement and found that any gains from having the cameras rigidly attached were more than offset by the reduced degrees of freedom for the positioning and orienting the cameras. Verging individually mounted cameras by separately tilting each one is easy. This is not possible with multiple

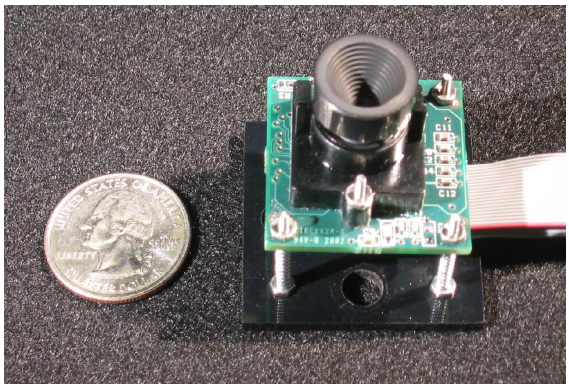

Figure 3.2: A camera tile.

sensors on the same flat printed circuit board without expensive optics. Manufacturing variations for inexpensive lenses and uncertainty in the placement of image sensor of a printed circuit board also cause large variations in the orientation of the cameras. The orientations even change as the lenses are rotated for proper focus. Correcting these variations requires individual mechanical alignment for each camera.

The final camera tile is shown in figure 3.2. Two meter long ribbon cables carry video, synchronization signals, control signals, and power between the tile and the processing board. The tile uses M12x0.5 lenses and lens mounts, a common size for small board cameras (M12 refers to the thread pitch, and 0.5 to the radius of the lens barrel in centimeters). The lens shown is a Sunex DSL841B. These lenses are fixed focus and have no aperture settings. For indoor applications, one often wants a large working volume viewable from all cameras, so I chose a lens with a small focal length, small aperture and large depth of field. The DSL841B has a fixed focal length of 6.1mm, a fixed aperture F/# of 2.6, and a diagonal field of view of 57°. For outdoor experiments and applications that require narrow field of view cameras, we use Marshall Electronics V-4350-2.5 lenses with a fixed focal length of 50mm, 6° diagonal field of view, and F/# of 2.5. Both sets of optics include an IR filter.

The camera tiles measure only 30mm on a side, so they can be packed very tightly. They are mounted to supports using three spring-loaded screws. These screws not only hold the cameras in place but also let one fine-tune their orientations. The mounts let us

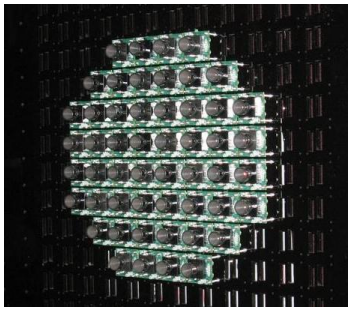

Figure 3.3: 52 cameras on a laser-cut acrylic mount.

correct the direction of the camera's optical axis (which way it points), but not rotations around the axis caused by a slightly rotated image sensor.

The purpose of the mounting system is not to provide precise alignment, but to ensure that the cameras have enough flexibility so we align them roughly according to our needs, then correct for variations later in software. Being able to verge the cameras sufficiently is critical for maintaining as large a working volume as possible, or even ensuring that all cameras see at least one common point. Image rotations are less important because they do not affect the working volume as severely, but as we will see later, they do limit the performance of our high speed video capture method.

For densely packed configurations such as in figure 3.3, the cameras are mounted directly to a piece of laser cut acrylic with precisely spaced holes for cables and screws. This fixes the possible camera positions but provides very regular spacing. Laser cutting plastic mounts is quick and inexpensive, making it useful for prototyping and experimenting. For more widely spaced arrangements, the cameras are connected to 80/20 mounts using a small laser-cut plastic adaptor. 80/20 manufactures what they call the "Industrial Erector Set"®, a T-slotted aluminum framing system. With the 80/20 system, we can create different camera arrangements to suit our needs. Figure 3.4 below shows some of the arrangements built with this system.

Figure 3.4: Different array configurations using 80/20 mounts.

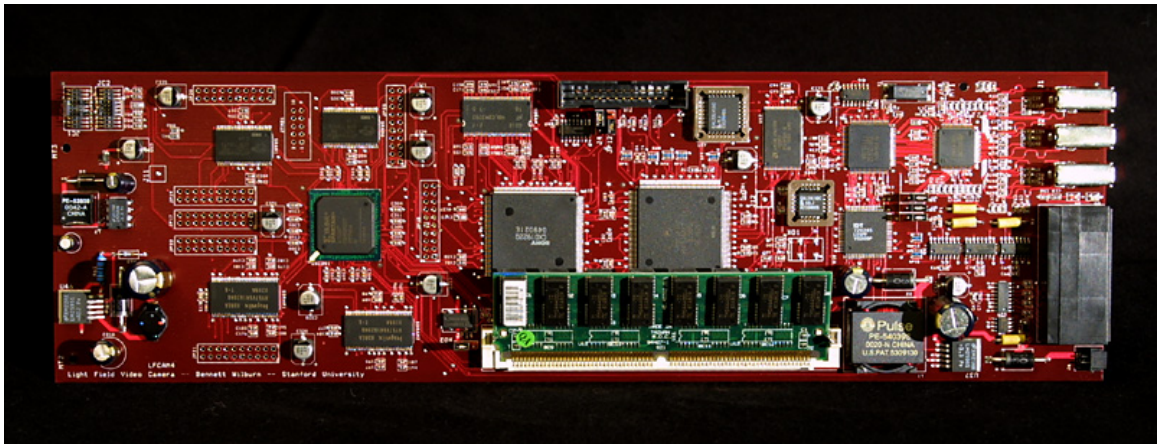

Figure 3.5: Camera processing board

3.3.2 Processing Boards

The processing board for each camera represents the bulk of the cost, functionality and design effort for the camera array. The board can capture 20 frames of raw video to local memory and stream raw or MPEG-compressed video to the host PC. Because there are many ways to design a board for a given functionality, I will cover the functionality and hardware choices at a high level and delve into details only for aspects of the design that enable unique features of the array (such as the timing accuracy) or made it particularly useful for research purposes.

Figure 3.5 shows the processing board. Each of these boards manages just one image sensor. The major components were chosen to maximize performance at reasonable design and manufacturing cost. The SONY CXD1922Q MPEG2 encoders were obtained at a discount for this project. I chose a Texas Instruments chipset for the IEEE1394 interface because they were a clear market leader at the time. These chips claim a glueless interface to Motorola Coldfire processors, so I selected a Motorola MCF5206E processor to manage the IEEE1394 chipset and MPEG encoder. I included 32MB of EDO DRAM, the maximum the processor supports, because this sets the limit on how much raw data each camera can capture. An IDT72V245 8KB FIFO buffers data between the IEEE1394 streaming interface and the rest of the board.

A Xilinx XC2S200 Spartan II FPGA along with a pair of 64Mbit SDRAMs and a pair of 4Mbit SRAMs provides glue logic between the different chips and some low-level processing power. FPGAs, (Field Programmable Gate Arrays), are configurable logic chips. They do not fetch instructions like microprocessors. Instead, they are a sea of identical, generic logic blocks with programmable functions and interconnect. A bitfile streamed into the FPGA configures the function of each logic block and the connections between blocks. The bitfile is specified using a behavioral language like Verilog. This specification is more complicated than programming a processor in C for the designer, but is necessary to handle non-standard data interfaces and to process video in real-time.

Figure 3.6 shows the data flow through the processing board. To stream raw video, the FPGA routes the incoming video straight through to the IEEE1394 chipset for isochronous transfer back to the host PC. For MPEG2 compressed video, the sensor data is sent to

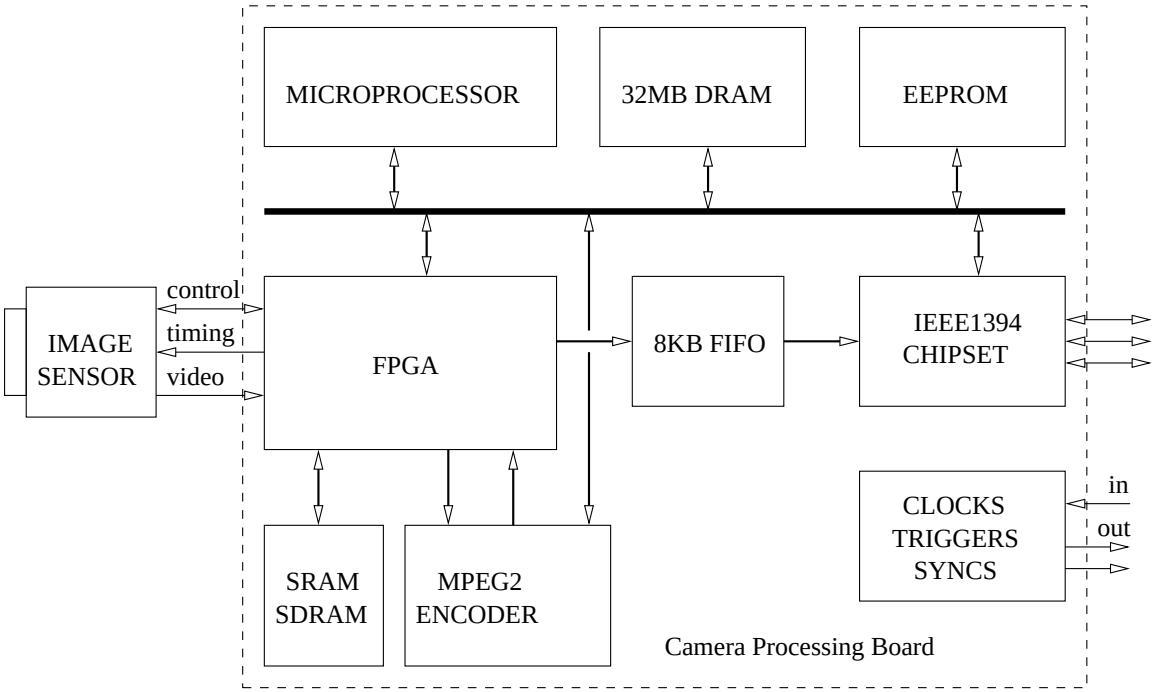

Figure 3.6: Camera processing board block diagram

the MPEG2 encoder, and the resulting bitstream is routed through the FPGA back to the IEEE1394 chipset. The FPGA can also simultaneously stream video and capture up to twenty uncompressed frames to the 32MB system memory using Coldfire-assisted DMA (Direct Memory Access) transfers. The Coldfire initiates all memory accesses to the 32MB DRAM. Without DMA transfers, the Coldfire would have to read the raw data from the FPGA, then write it back to the DRAM using the same data bus. In a DMA transfer, the microprocessor signals a write to the DRAM, but the data is provided directly by the FPGA, eliminating the unnecessary read.

3.3.3 System Timing and Synchronization

The precise timing control over each camera in the Stanford Multiple Camera Array opens up new research avenues that will be explored in the rest of this thesis. The cameras in the 3D-Room and Virtualized Reality are synchronized using “Genlock,” the most common off-the-shelf solution for camera synchronization. Genlock is an analog protocol that

provides synchronization with coincident triggers, not arbitrary timing, and is too costly for inexpensive cameras. This is why the Dynamic Light Field Viewer, constructed of inexpensive webcams, is not synchronized.

The Stanford Multiple Camera Array provides accurate timing with arbitrary phase shifts between camera triggers using the FPGAs and dedicated clock and trigger lines that run through the entire array. The one root board in the array generates its own 27MHz clock and sends it to two children via CAT5 cables, which then buffer the clock and send it to two more children, and so on. The root board is identical to the other camera boards except for the code in one GAL and a single jumper setting. A PLL on each board uses the system clock to generate duty-cycle corrected, 27MHz and 54MHz clocks. The MPEG encoders require a 27MHz clock, but we run the microprocessors and FPGAs twice as fast to maximize their performance.

The clock is not used for data transmission between boards, so delay from camera to camera is unimportant. The shared clock only ensures that all boards are frequency-locked. It is possible that the duty cycle degrades with each buffering of the clock, but the board components require a $45\% - 55\%$ duty cycle. This is one reason the cameras propagate a 27MHz clock, then double it on the board with a PLL. Preserving the 27MHz duty cycle is also easier because the period is twice as long, and the PLL ensures a 50% duty cycle on the processing boards. Propagating the system clock using a minimal depth binary tree routing topology preserves the duty cycle by ensuring a bound of $\log_2 N$ hops from the root board to any camera, as opposed to N-1 for a daisy-chained system. We also invert the sense of the clock each time it is buffered, so systematic duty cycle offsets in the clock propagation circuitry are roughly cancelled. In practice, this system works quite well. The maximum depth of our tree for a 100 camera array is eight levels, and we have tested daisy-chained configurations with more than 16 cameras with no problems.

Frequency-locked system clocks prevent our cameras from drifting relative to each other. The FPGAs on each board generate vertical and horizontal synchronization signals for the image sensors and the MPEG2 encoders. The encoders actually drive the system timing because their requirements are very exact—NTSC timing based on a 525 line-per-image video with a 27MHz clock. The FPGAs timing units run the image sensors and MPEG encoders at exactly the same frame rate. With a common system clock, this means

that all the sensors and encoders run at exactly the same frequency.

Synchronization is more than just preventing frequency drift. We also need to set the relative timing of the cameras' exposures and the frame on which the cameras start and stop capturing video. The timing of IEEE1394 transfers, especially from multiple networked PCs, is simply too uncertain for the accuracy we need in our system, so I put that control directly into our hardware. The same CAT5 cables that carry the clock transmit global triggers from the root board to the rest of the array. These signals route directly to the FPGAs on the boards. They control the initial synchronization or staggering of the sensor shutter timing and the frame-accurate start of all video streaming or snapshots.

Video timing initialization is a good example of how to execute timing-sensitive commands for the camera array. The FPGAs use two video counters to drive the vertical and horizontal inputs of the image sensors and MPEG2 encoders. The *pixel counter* rolls over when it reaches the number of pixels in a line, causing the *line counter* to increment. The line counter rolls over at 525 lines, signaling a new frame. Once these counters have been initialized, they run without drift across the entire array because of the common system clock. The reset values for the line counters is a programmable register on the FPGA, accessible via an IEEE1394 command to the board.

To set up arbitrary time shifts between cameras, we program different values into the line counter reset registers, send a command which instructs the boards to reset their counters on the next rising trigger signal, and then tell the root board to assert the trigger. All of the setup for all boards is done using IEEE1394 reads and writes, but the order to reset their timers, which must be executed at the same time by all cameras, is sent just to the root board. The root board then asserts the trigger signal for the entire array. The inaccuracy of the camera synchronization is limited to the electrical delay propagating the trigger to all of the boards. For the 100-camera array, this is less than 150ns, or roughly the time to scan out four pixels from the image sensor.

3.3.4 Developer Interface to the Boards via IEEE1394

A flexible mounting system and low-level camera control make it easy to experiment with different applications, but we also need a development environment that facilitates adding

new features to the cameras. I took advantage of the IEEE1394 bus to make prototyping quick and easy. After power-up or a board reset, the Coldfire executes simple boot code which configures the microprocessor memory and the IEEE1394 interface. The host PC then downloads FPGA bitfiles and a more sophisticated Coldfire executable from the PC via IEEE1394. Adding new camera features is just a matter of compiling these new files and does not require modifications to the physical hardware (i.e. programming GALs or boot ROMs). This is critical for an array of 100 cameras.

A simple bootloader and downloadable executables and bitfiles makes iterating design changes easy. Other goals for the design environment were to implement as much as possible on the host PC using a familiar C development environment, keep the downloaded executable simple, and expose as much of the camera state as possible to the user. Once the final executable has been downloaded, the important state in each camera is mapped into its IEEE1394 address space. Using standard IEEE1394 reads and writes, one can access the full 32MB of DRAM attached to the processor, all of the control registers in the MPEG2 encoder and IEEE1394 chipset, configuration registers programmed into the FPGA, and control registers for the cameras themselves. This keeps the developer API for the array simple—just IEEE1394 reads and writes—and makes it easy to track the state of the board (what has been programmed into registers in the FPGA, image sensor, MPEG encoder) from the host PC application.

3.3.5 Image Processing on the FPGA

Raw image data from the cameras almost always need to be processed before they can be used. With this in mind, I designed the cameras for reasonable cost with as powerful an FPGA and as much associated memory as I could. As one example of the potential of the FPGA, we have implemented Bayer demosaicing of the raw sensor data using the Adaptive Color Plane Interpolation algorithm of [39]. This method needs access to five adjacent lines of raw image data, meaning the FPGA must buffer four lines of the image. Rather than use the external memory, we use built-in BlockRAMs on the Spartan-II. These RAMs can be used for FIFOs with up to 511 entries, so for this exercise we processed only 510-pixel-wide images. We have also implemented arbitrary geometric warps for color images

using lookup tables with eighth-pixel accurate coordinates and bilinear interpolation. We currently use this for keystone corrections so we can view live synthetic aperture video.

3.3.6 Limits due to IEEE1394 Arbitration

The maximum isochronous (streaming) data transfer rate for IEEE1394 is 320Mb/s. The standard method for streaming data from many different IEEE1394 devices is to assign each one a different isochronous channel number and a fixed portion of the bandwidth in each 1394 cycle, but this turns out to be a poor strategy. One device streaming data can achieve the maximum rate, but with many nodes, arbitration overhead will reduce the maximum bandwidth. Devices must arbitrate before every isochronous packet is sent, and arbitration takes longer with more nodes because signals must propagate from all nodes up to the root and then back. Moreover, each IEEE1394 packet also has an overhead of three quadlets (four bytes each) to describe the packet (data length, isochronous channel number, data correction, and so on).

For an MPEG data rate of 4Mb/s (the default for our encoders), each camera must transfer 66 bytes every 125us isochronous cycle. IEEE1394 packet lengths must be multiples of four, meaning each camera must be configured to stream 68-byte packets. Adding twelve bytes for packet overhead produces an 80-byte packet. At most, 51, 80-byte packets would fit in the maximum of 4096 bytes per cycle. After arbitration overhead, we have found that we can stream only 26, 4Mb/s cameras reliably. We have verified with an IEEE1394 bus snooper that arbitration overhead is indeed the culprit preventing more packets on the bus.

Streaming such small packets each cycle from every camera produces a data file on the host PC that is very fragmented and thus hard to process. Programs must scan through the data 80 bytes at a time to look for data from a specific camera. To fix this difficulty and the overhead issues, we attempted to implement an isochronous transfer scheme in which each camera sends a full 4096-byte isochronous packet every N cycles. Each camera counts isochronous cycles using the cycle done interrupt from the IEEE1394 chipset. Access to the bus passes round-robin through the array, and each camera is responsible for attempting to send data only on its dedicated cycle.

We cannot implement this scheme with 4KB packets because we have a one-cycle uncertainty in our control over the IEEE1394 bus. Instead, we set the cameras to transmit a 2KB packet on their designated cycle. If a camera is late one cycle and transmits at the same time as its successor, the data will still fit in the cycle and no errors will occur. This optimization makes real-time applications much easier by fragmenting the data less and slightly increases the number of cameras we can stream simultaneously on the bus. We are still investigating what is necessary for cycle-accurate control of the isochronous interface.

3.3.7 Host PCs

Given the limit of roughly thirty cameras per IEEE1394 bus, 100 cameras require multiple IEEE1394 buses. At this point, we run into another limit on our data transfer bandwidth—the 33MHz PCI bus in our computers. The IEEE1394 adaptor is a PCI device, and transferring data from it to our hard drives requires two PCI transfers, one from the adaptor to main memory, and a second to the hard drives. The transfers are both DMA-assisted, but here the role of the DMA is just to free the processor, not to reduce PCI bus bandwidth. The maximum theoretical bandwidth for 33MHz PCI is 133MB/sec, but the maximum sustained data transfer rate is much less. An aggressive estimate of 80MB/s means we are limited to one IEEE1394 bus per computer. Thus, we need one computer for every thirty cameras.

The currentl implementation of the array with one hundred cameras uses four host PCs which each manage a separate IEEE1394 bus. We run a copy of the array software on each PC using a client/server setup where the server is the PC connected to the root board of the array. The server issues all commands for downloading executables and code, setting up timing, programming registers on the image sensors, recording MPEG2 compressed video, uploading stored snapshots of raw images, and so on. The only command that cannot always be run from the server is viewing live uncompressed video from the cameras—rather than trying to send live video across the network from PC to PC, raw video is always viewed on the host PC for a given camera's IEEE1394 bus. We use a DVM switch to access all of the machines from one keyboard and monitor.

The host PCs have been optimized for our applications but are now somewhat out-of-date. They use IEEE1394 PCI cards and striped IDE hard drives to write incoming video

to disk as fast as it arrives. The PCs run RedHat Linux using the experimental IEEE1394 drivers, with one modification. The IEEE1394 specification allows up to 64 isochronous channels on a bus, but the Linux drivers currently support only four. Each camera in our system needs its own isochronous channel, so I modified the drivers to support the full 64 channels. Without this capability, our cameras would have to stream on the same isochronous channel and insert the camera number into a header in every streaming packet. More importantly, we would have to schedule the camera data transfer explicitly instead of relying on the IEEE1394 chipsets.

3.3.8 Design Environment

The choice of operating systems and design environments can be a matter of taste and is not critical to the performance of our architecture. I would like to briefly mention some choices that turned out to be both inexpensive and powerful, and to acknowledge some of the open source software tools that made our work easier. One decision that worked out well was using Jean Labrosse's μC/OS-II real-time operating system for our embedded microprocessors. The operating system is light-weight and easily ported. It costs a mere $60 and comes with a book that describes every line of the code.

Linux was helpful because the open source community developed some useful resources early. We used a cross-compiler for Linux and Coldfire processors provided by David Fiddes (http://sca.uwaterloo.ca/www.calm.hw.ac.uk/davidf/coldfire/gcc.htm). At the time when we were doing most of the embedded processor code, GDB supported remote-debugging for the Coldfire using the Background Debug Mode port, while inexpensive Windows tools for the Coldfire did not. More information on the Coldfire MCF5206E and its Background Debug Mode can be found at [40]. Debugging our embedded IEEE1394 drivers and the application running on the host PCs was much easier in Linux because we could step through source code for working applications to see how our devices were expected to behave and how other applications accessed the bus.

Open source code was critical for getting isochronous streaming working with more than four cameras. At the time, Windows did not yet have IEEE1394 drivers (this was before Windows 2000), and some commercial IEEE1394 drivers did not even implement

Figure 3.7: The Stanford Multiple Camera Array

isochronous transfers, let alone streaming from many nodes. Fortunately, access to the source code for the IEEE1394 drivers allowed me to implement the driver modifications described earlier that allowed DMA transfers from PCI IEEE1394 adaptors to main memory from multiple isochronous channels. For many aspects of this project, we were able to leverage the work of others to get our machinery running sooner.

3.4 Final Specifications

Figure 3.7 shows the Stanford Multiple Camera Array set up in a widely spaced configuration. This photograph shows 125 cameras, but we have only 100 cameras up and running. Aside from that detail, the system as shown is accurate. The cameras run off four PCs, one for each of the blue cabinets holding the camera processing boards. The video and images for the applications and analysis in the rest of this thesis were all acquired by this

hardware or a subset of it in varying configurations. We can capture up to two minutes of video from all of the cameras. This rather artificial limit is due to the 2GB file size limit of our operating system, but we have not yet tried to capture longer events. The total cost of the array is roughly $600 per board.

3.5 Future Work

As the rest of this thesis will show, we have used the array in many different configurations for several different purposes. These experiences have identified areas of the array that could use improvement. I will briefly discuss them here before moving on to the applications.

Mounting and aiming cameras is by far the most time-consuming task for reconfiguring the array. The mounting system is flexible, but very labor-intensive. A simple mechanical mount that snapped in place would be nice, as would one that allowed electronic control over the camera pan and tilt. One simple but useful addition would be an LED on the front of each camera. For any new camera configuration, we need to identify which is which before we can start aiming them. Right now, we identify cameras by trial and error, but we have fabricated a new set of camera tiles with an LED that we intend illuminate from the host to make manually or even automatically mapping the camera layout much simpler. Once we have identified cameras, we can track them using unique IDs on the processing boards that can be queried from the host PCs. The detachable sensor tiles do not have IDs. If they did, we could also just label the tiles with their ID and manually determine the camera layout. Unique camera IDs might prove useful later for keeping records of sensor radiometric properties.

The sensors in the camera array have an electronic rolling shutter, analogous to a mechanical slit shutter. In chapter 5, I discuss the electronic rolling shutter, the distortions it introduces for fast-moving objects, and how to partially overcome them. Interactions between the shutter and geometric calibration make it impossible to completely overcome the artifacts. Furthermore, synchronizing the cameras with different illuminators is not possible. If I were to design the array again, I would use sensors with snapshot shutters.

The array has one hundred synchronized video cameras, but not a single microphone.

Synchronizing one or more microphones with the array would enable more interesting multimedia content.

Finally, this camera array design is now several years old. I use four PCs to capture the video data, but it might be possible now to use one multiprocessor PC with dual PCI-X buses to single-handedly capture all of the array data. Currently, any real-time application I would like to implement must account for only one quarter of the array data being available on any one machine. Running the entire array of one host would fix that and also eliminate all of the network synchronization in our host PC software. Faster processor buses like PCI-X are only one way that technologies are improving. If I were to redesign the array today, I could build it with more efficient video compression technologies like MPEG-4 and new alternatives for high-speed buses, notably 800 Mb/s IEEE1394b and USB 2.0. As data transfer rates increase, new arrays could exploit improvements in inexpensive image sensors to capture video with greater resolution and higher dynamic range.

Chapter 4

Application #1: Synthetic Aperture Photography

Synthetic aperture photography (SAP) is a natural use for a large camera array because it depends on a large number of input images. As we will see, SAP is also a good starting application because although it requires accurate geometric camera calibration, it is relatively forgiving of radiometric variations between cameras. The rest of this chapter describes the synthetic aperture method in detail and explains how we geometrically calibrate our cameras. I show results using the array to create synthetic aperture photographs and videos of dynamic scenes, including a demonstration of live SAP video with interactive focal plane adjustment that takes advantage of the processing power in our cameras.

4.1 Description of the Method

The aperture of a camera determines its depth of field and how much light it collects. Depth of field refers to the distance from the focal plane at which objects become unacceptably out of focus in the image. This could be the point at which the blur is greater than one pixel, for example. The larger the aperture, the narrower the depth of field, and vice versa. This can be exploited to look through partially occluding objects like foliage. If a camera with a very large aperture is focused beyond the occluder, objects at the focal depth with be sharp and in focus, while the objects off the focal plane will be blurred away. Although only a

portion of the light from the object of interest penetrates the foreground partial occluder, their contributions all add coherently when focused by the lens on the image plane. The result is an image of the object with reduced contrast.

Rather than actually building a camera with a one meter wide aperture, synthetic aperture photography samples the light entering the effective aperture using an array of cameras. Levoy and Hanrahan pointed out that using a camera with a given aperture size, it is possible to simulate images taken with a larger aperture by averaging together many adjacent views, creating what they call a "synthetic aperture" [5]. Isaksen, et al. created a synthetic aperture system using less dense camera spacings [6]. Because they used a single translating camera to capture images for their experiments, they were limited to static scenes. They showed with synthetic data that they could see through objects in front of their focal surface. We are the first to use a camera array to create synthetic aperture photographs and videos.

Figure 4.1 shows how a basic lens works. Light from a focal plane in the world is focused by the lens onto an image plane in the camera. If an object, represented by the dashed line, is placed in front of the focal plane, the light striking a given point on the image plane comes from a neighborhood on the object and not one single point, causing blur. As the object moves farther from the focal plane, the blur increases.

Figure 4.2 shows how a smaller aperture cuts out rays from the periphery of the lens. Eliminating these rays decreases the area on the object over which we collect light for a given point in our image, meaning the object will look less blurry in the image. The depth of field has increased—the object can be farther away from the focal plane for the same amount of blur. Conversely, a very large aperture will result in a very small depth of field, with object rapidly becoming out of focus as their distance from the focal plane increases.

As depicted in figure 4.3, synthetic aperture photography digitally simulates a wide aperture lens by adding together the appropriate rays from multiple cameras. The camera array and processing digitally recreate the function of the lens by integrating the light from rays diverging from a point on the focal plane and passing through the synthetic aperture. To do this, we need some form of geometric calibration to determine which pixels in our images correspond to rays from a given point on the focal plane.

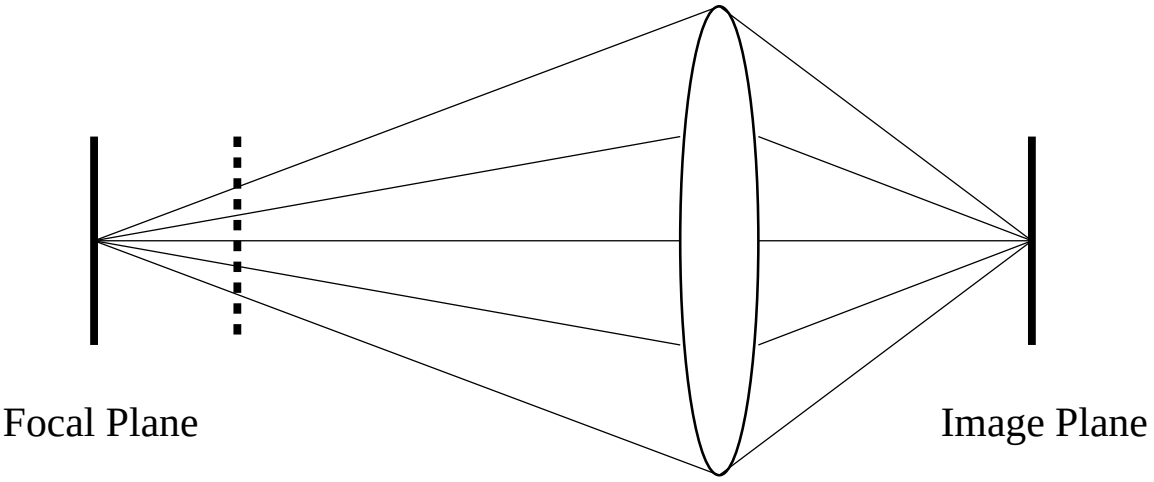

Figure 4.1: A basic lens system. Rays leaving a point on the focal plane are focused by the lens onto a point on the image plane. For an object (represented by the dashed line) off the focal plane, rays emanating from some patch of the surface will be focused to the same point in the image, causing blur.

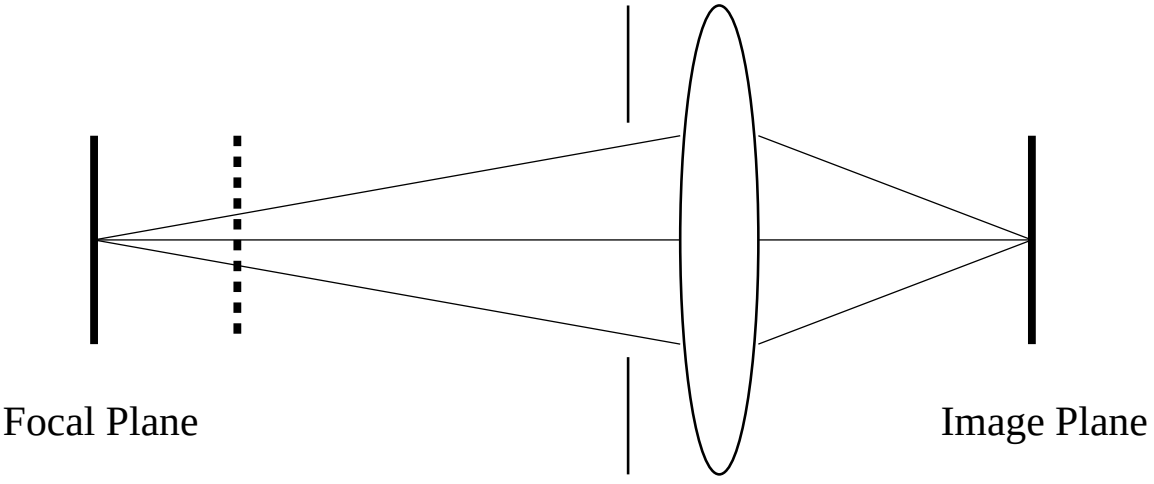

Figure 4.2: A smaller aperture increases depth of field. For an object off the focal plane, the smaller aperture means light from a smaller area of the object's surface will reach the image plane, reducing blur.

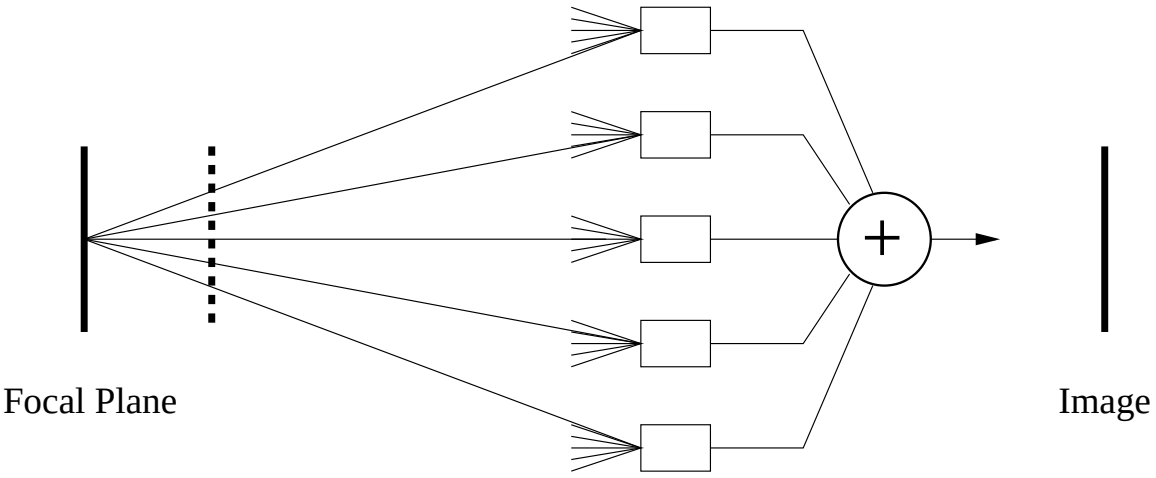

Figure 4.3: A synthetic aperture camera uses many cameras to sample the light crossing the synthetic aperture. It then digitally simulates a lens by integrating measurements for light arriving at the cameras from the same point on the desired focal plane.

4.2 Geometric Calibration

The degree of calibration required for synthetic aperture photography depends on the desired focal surfaces. As Isaksen et al. [6] note, synthetic aperture photography is not limited to a single focal plane–one could create an image with different regions focused at different depths, or use curved or otherwise non-planar focal surfaces. Arbitrary surfaces require full geometric camera calibration–a mapping from pixel locations in each image to rays in the world. If we restrict ourselves to sets of parallel focal planes (similar to a regular camera), then much simpler calibration methods suffice [7]. Here, I review camera models and geometric camera calibration, then explain the simpler homographies and plane + parallax calibration we use for synthetic aperture photography and the other multi-camera applications in this thesis.

4.2.1 Full Geometric Camera Calibration

Full geometric camera calibration determines how the three-dimensional (X,Y,Z) "world coordinates" of a point in our scene map to the two-dimensional (x,y) pixel coordinates of its location in an image. In practice, this is done using a mathematical pinhole camera

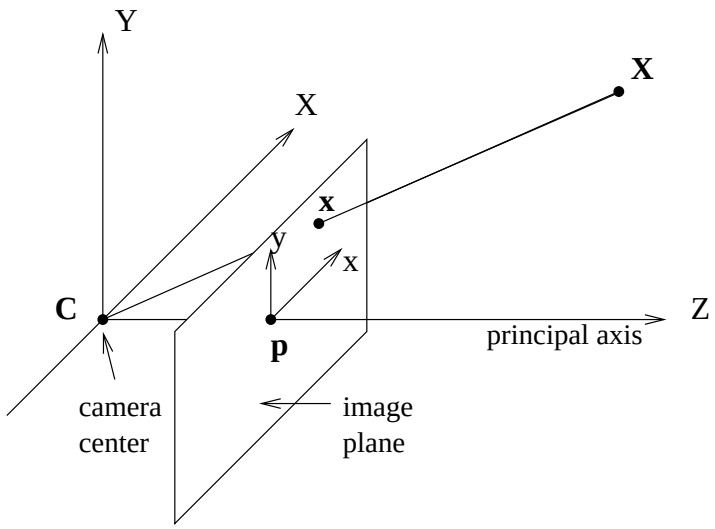

Figure 4.4: The pinhole camera model. The image of a world point is at the intersection of the image plane with the line joining the point and the camera center.

model [41], shown in figure 4.4. The image of a world point is at the intersection of the image plane with the line joining the camera center and the world point. This operation is called a "projection," and the camera center is also known as the "center of projection." The line passing through the camera center and perpendicular to the image plane is called the "principal axis." The intersection of the principal axis and the image plane, **p**, is called the "principal point."

The pinhole camera model is divided into the intrinsic and extrinsic parameters. The intrinsic parameters relate the location of points in the camera's coordinate system to image coordinates. In the camera's coordinate system, the camera center is the origin, the z-axis is the principal axis, and the x and y axes correspond to the image plane x and y axes, as shown (the image plane x and y axes are assumed to be orthogonal). In these coordinates,

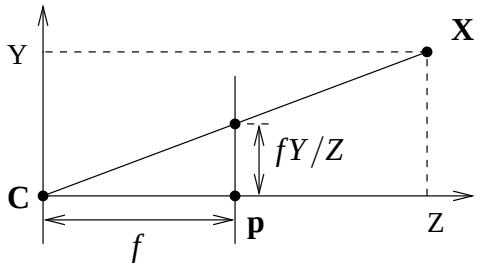

Figure 4.5: Pinhole camera central projection. In camera coordinates, the mapping from any point to its projection on the image plane is $(X,Y,Z) \rightarrow (fX/Z, fY/Z)$

the mapping from any point to its projection on the image plane is simply

$$(X,Y,Z) \rightarrow (fX/Z, fY/Z)$$

Here, f is the focal length, the distance from the camera center to the image plane. Figure 4.5 shows this in one dimension.

The projection just described gives the (X,Y) coordinates of the projection of a point onto the pinhole camera image plane. To relate this to image coordinates, we first need to divide these coordinates by the pixel size. Equivalently, we can express the focal length f in units of the pixel size. To account for the shift between the $(0,0)$ image coordinate (which is usually at the bottom left corner of the image) and the image of the principal axis (which is roughly in the center), we add a principal point offset (p_x, p_y). This gives the mapping

$$(X,Y,Z) \rightarrow (fX/Z + p_x, fY/Z + p_y)$$

The extrinsic properties of a camera, or its "pose", describe its location and orientation in world coordinates. Mathematically, it is a transformation between world and camera coordinates. If the camera center is **C**, and the rotation matrix **R** is a 3x3 rotation matrix that represents the camera coordinate frame orientation, then a world coordinate $\mathbf{X}_{world}$ maps to camera coordinates $\mathbf{X}_{cam}$ according to

$$\mathbf{X}_{cam} = \mathbf{R}(\mathbf{X}_{world} - \mathbf{C})$$

Letting $\mathbf{t} = -\mathbf{RC}$, this can be expressed more simply as:

$$\mathbf{X}_{cam} = \mathbf{R}\mathbf{X}_{world} + \mathbf{t}$$

The extrinsic parameters for the pinhole camera model have six degrees of freedom– three for the translation t, and three for the rotation matrix $\mathbf{R}$. Although the matrix has nine entries, there are only three degrees of freedom, corresponding to roll, pitch and yaw. The intrinsic properties of the camera have three degrees of freedom: the focal length f, and the location of the principal point (x_p, y_p). More general camera models that account for non-square pixels will use two focal lengths, f_x and f_y, to express the focal lengths in terms of the pixel width and height. Finally, the most general models will also include a "skew" parameter s that accounts for non-orthogonal image axes. This will not happen for normal cameras, so this parameter is usually zero. Neglecting s, we now have a ten degree of freedom model that relates world coordinates to image coordinates by transforming world to camera coordinates, then projecting from camera to image coordinates.

Configuring cameras to exactly match a specific camera model is nearly impossible, so in practice one always sets up the cameras and then calibrates them to determine the model parameters. Much work has been done on how to calibrate cameras from their images. Early approaches used images of a three-dimensional calibration target [42, 43]. The calibration targets have easily detectable features, like the corners of a black and white checkerboard pattern, at known world coordinates. Zhang developed a method that requires multiple images of a planar calibration target [44]. Planar targets are more convenient because they can be easily created using a laser printer. All of these methods attempt to minimize the error between imaged feature coordinates and coordinates predicted from the model.

To perform full calibration for our array, we use a method developed by Vaibhav Vaish that extends Zhang's method to multiple cameras [45]. As in Zhang's method, the input to the calibration is multiple images of a planar target with known two-dimensional coordinates in the plane. Vaish has developed a very robust feature detector that automatically finds and labels the corners of squares on our target. Typical results for the feature detector are shown superimposed on an image of the target in figure 4.6. The target is designed to

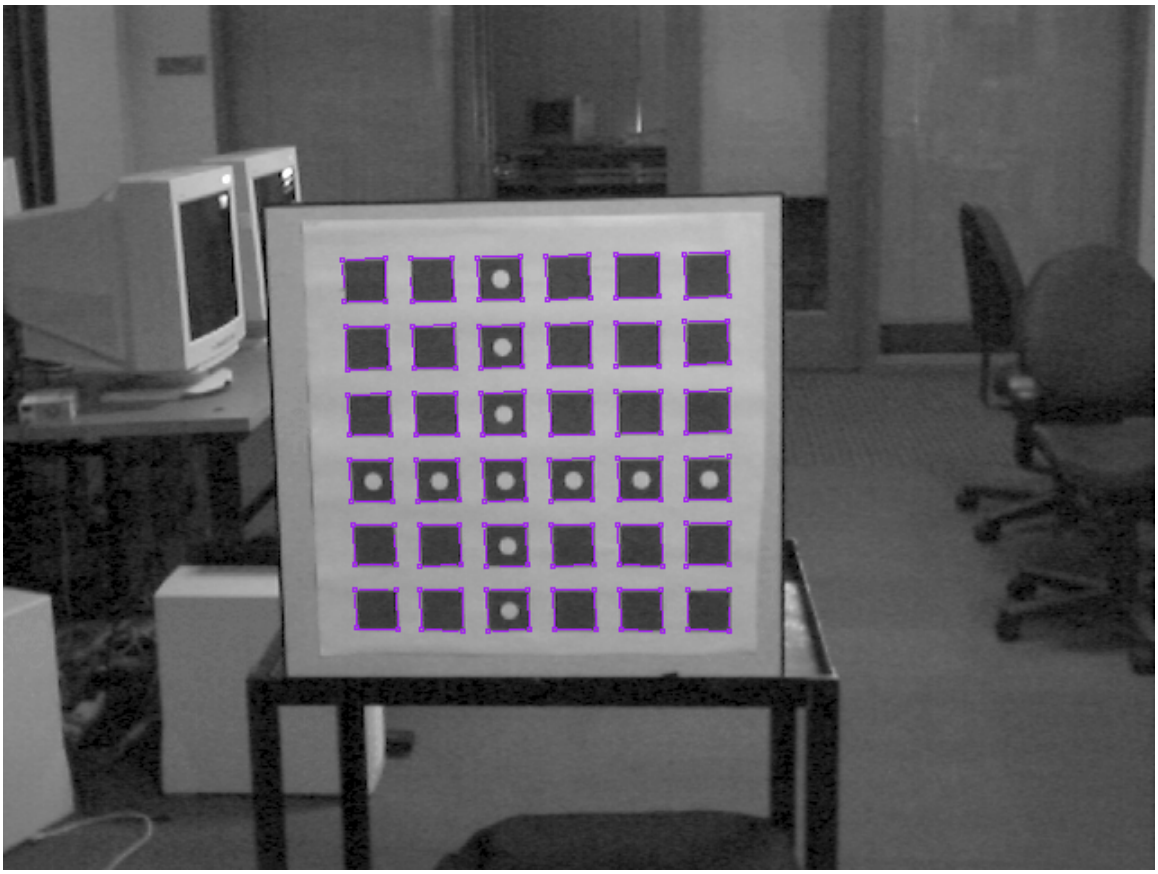

Figure 4.6: Our robust feature detector automatically detects and labels feature points on our calibration target.

have uniquely identifiable features even if the entire target is not visible, a common occurrence for our large array. Using the target-to-image correspondences, we get an initial estimate of the camera model parameters by independently calibrating each camera using Zhang's method. This estimate is used to initialize a nonlinear optimization (bundle adjustment) that solves for all parameters simultaneously. We typically get an RMS pixel projection error of 0.3 pixels with this method.

4.2.2 Planar Homographies

Full geometric calibration for an array of one hundred cameras can be quite challenging. For many uses of the array, being able to reproject images from the image plane to some other plane in the world is sufficient. Synthetic aperture photography, for example, only requires a mapping from the focal plane to the camera image planes. Similarly, the two-plane parametrization used in light field rendering aligns images from all views onto a common object plane [5]. Some approaches to multi-view stereo also use a space-sweep framework, once again aligning camera images to planes in the world [46, 47].

The mapping between planes is defined by a projection through the camera center. Corresponding points on the two planes lie on a line passing through the camera center. This relationship, called a 2D projective transformation or planar homography, can be described using homogeneous coordinates as a 3x3 matrix with eight degrees of freedom [41]. Furthermore, it can be computed independently for each camera directly from image measurements, with no knowledge of the camera geometry. Figure 4.7 shows a typical use of a planar homography to align images to a reference view. In this example, we determine the mapping directly by placing our planar calibration target on the plane to which we will align all images. To create a synthetic aperture image focused on the plane of the target, we simply add the aligned the images from all cameras.

4.2.3 Plane + Parallax Calibration

For many applications, aligning images to a single plane is insufficient. For example, we would like to focus at different depths for synthetic aperture photography, or select different object planes for light field rendering, without computing a new set of homographies. This can be done using “plane + parallax” calibration. Although the projections could be computed using full geometric calibration, for planar camera arrays and fronto-parallel focal planes, plane + parallax calibration is simpler and more robust [7].

To calibrate using plane + parallax, we first align images from all of our cameras to a reference plane that is roughly parallel to the camera plane. We do this as before, using images of a planar calibration target set approximately fronto-parallel to the camera array. We designate a central camera to be the reference view and compute an alignment for it that

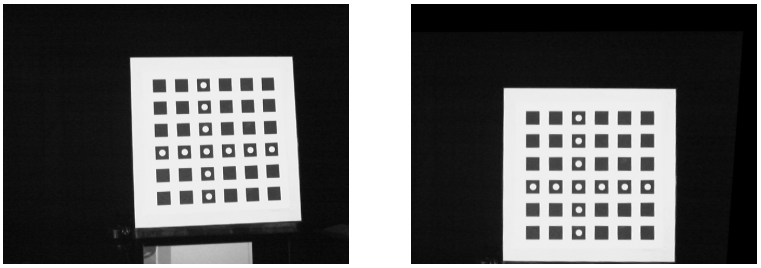

(a) (b)

Figure 4.7: Alignment using planar homographies. Using images of a planar calibration target, we compute a planar homography that aligns each image to a reference plane. (a) shows an image of the target from a corner camera of the array. (b) show the same image warped to the reference view. The planar target appears fronto-parallel in all of the aligned images.

makes the target appear fronto-parallel while perturbing the imaged target feature locations as little as possible. We then compute planar homographies that align the rest of the views to the aligned reference view [41]. At this point, all our images are aligned to a reference view as in figure 4.7.

In the aligned images, there is a simple relation between a point's distance from the reference plane and its parallax between two views. Figure 4.8 shows a scene point P and its locations $p_0 = (s_0, t_0)^T, p_1 = (s_1, t_1)^T$ in the aligned images from two cameras C_0 and C_1. Let Δz_p be the signed distance from P to the reference plane (negative for this example), Z_0 be the distance from the camera plane to the reference plane, and Δx be the vector from C_0 to C_1 in the camera plane. Define the *relative depth* of P to be $d = \frac{\Delta z_p}{\Delta z_p + Z_0}$. Given this arrangement, the parallax $\Delta p = p_1 - p_0$ is simply $\Delta p = \Delta x \cdot d$.

This has two important consequences:

- The parallax between aligned images of a single point off the reference plane is enough to determine the relative locations in the camera plane of all of the cameras. This is the heart of the plane + parallax calibration method. Typically, one measures the parallax of many points to make the process more robust.

- Once we know the relative camera locations, determining the relative depth of a point

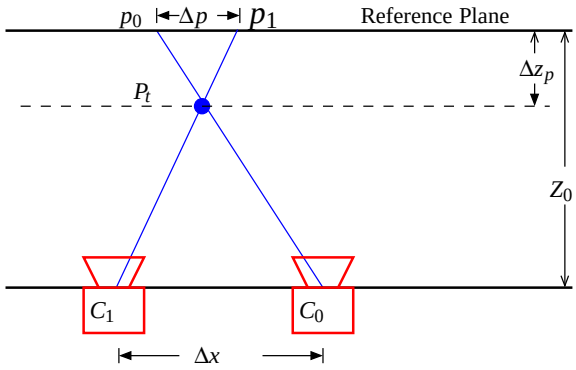

Figure 4.8: Planar parallax for planar camera arrays. A point P not on the reference plane has distinct images p_0, p_1 in cameras C_0, C_1. The parallax between these two is the product of the relative camera displacement Δx and the relative depth Δz_p.

in one view is enough to determine its location in all other views. We will use this later for spatiotemporal view interpolation.

Plane + parallax calibration plays a major role in most of the applications in this thesis. We use it in synthetic aperture photography to easily focus at different depths. Once we have aligned images to a plane at one depth, we can create synthetic aperture images focused at other depths by translating the images by some multiple of the camera displacements. For high speed videography, we align images from all of our cameras to one focal plane, and plane + parallax describes the misalignment errors we will see for objects not on that plane. Finally, the spatiotemporal view interpolation method uses plane + parallax calibration to estimate scene motion between images from several different cameras.

4.3 Results

The synthetic aperture images and videos I present in this chapter were enabled by our capture hardware and geometric calibration methods. Because we average images from all cameras to create each synthetic aperture image, streaming capture from all cameras was essential for the videos. For any dynamic scene, the cameras had to be synchronized to trigger simultaneously. Many of these images and videos were produced using full

Figure 4.9: Synthetic aperture sample input images. Because these images are averaged together, the obvious color variations will have little effect on the output images.

geometric calibration, before we knew that plane + parallax would be simpler and more effective. Regardless, they show that we can effectively combine the data from all of our cameras.

For synthetic aperture experiments, we use a setup similar to the tightly packed arrangement in figure 3.4. The cameras are mounted on 80/20 bars with an effective aperture that is one meter wide and slightly less than one meter tall. Using a setup similar to the one shown but with only 82 cameras, we took a snapshot of a scene with a partially occluding plant in the foreground. Three example input images are shown in figure 4.9. Figure 4.10 shows a sequence of synthetic aperture images created from this dataset. The focal plane starts in the conference room behind the plant and sweeps toward the camera. Note the different portions of the image in focus at different focal depths, and how the face of the person hiding behind the plant is revealed even though each input camera could see only tiny portions of his face. We also have the option of enhancing our results with standard image processing techniques. In figure 4.11, we have cropped out the face from the fourth image in the synthetic aperture image sequence and enhanced the contrast. Despite having a plant between all of our cameras and the person, his face is now clearly visible and recognizable (assuming you know Professor Levoy!). This is just the beginning of the possibilities of digitally improving our results. Isaksen et al., for example, mentioned the possibility of implementing passive depth-from-focus and depth-from-defocus algorithms to automatically determine the depth for each pixel.

Of course, we are not limited to synthetic aperture photography. We have also used

Figure 4.10: Sweeping the synthetic aperture focal plane. In this sequence of synthetic aperture images, the focal plane is swept toward the camera array. Objects visible at one focal depth disappear at others, allowing us to clearly see the person hiding behind the plant, even though he was mostly occluded in the input images.

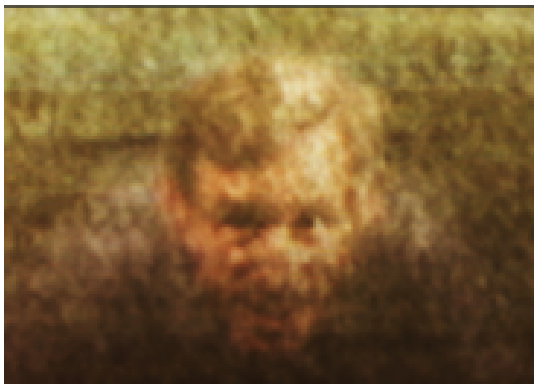

Figure 4.11: A synthetic aperture image with enhanced contrast.

Figure 4.12: Synthetic aperture video sample input images.

the array to create the world's first synthetic aperture videos of dynamic scenes. Using the same setup as before, we streamed synchronized, 4Mb/s MPEG video from all cameras to disk. The scene is three people walking behind a dense wall of vines. Three sample images from different cameras at the same time (with a person behind the vines) are shown in figure 4.12. These images actually make the situation seem worse than it really is. Viewing any one input video, one can tell that people are moving behind the vines, although it is not possible to tell who they are or what they are doing. I have included an example input video, sapvideoinput.mpg, on the CD-ROM accompanying this thesis.

The resulting synthetic aperture video is also on the CD-ROM, labeled sapvideo.mpg. In it, we see the three people moving behind the wall of vines and some of the objects they are carrying. Example frames are shown in figure 4.13.

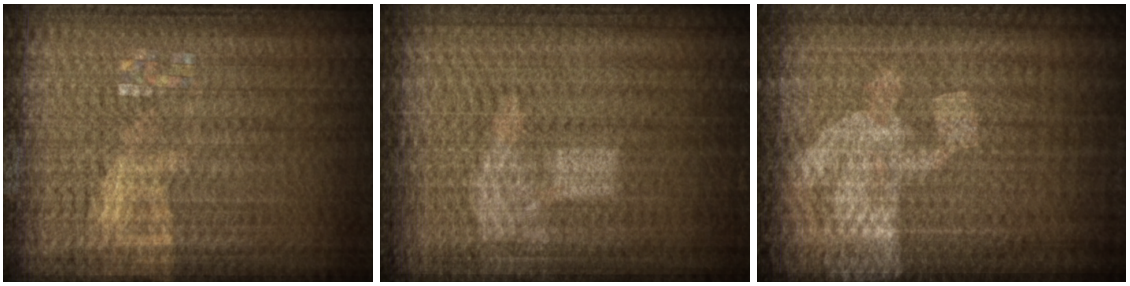

Figure 4.13: Frames from a synthetic aperture video.

The results presented so far have been generated off-line, but for surveillance applications, we would like to view live synthetic aperture video while interactively sweeping the focal plane. Using plane + parallax calibration, we can sweep the focal plane back and forth by translating the keystoned images before we add them together. This is the first real-time application we have implemented with the array, and the first demonstration of the value of using the FPGAs for low-level image processing. Instead of the PCs warping and shifting all the images, the cameras perform these operations in parallel before compressing and transmitting the video. The FPGA applies the initial homography using a precomputed lookup table stored in its SDRAM, then shifts the warped image before sending it to the MPEG compression chip. The PCs decode the video from each camera, add the frames together, and send them over a network to a master PC. The master sums the images from the other PCs and displays the synthetic aperture video.

The video livesap.avi on the companion CD-ROM demonstrates this system in action. It shows video from one of the cameras, a slider for interactively changes the focal depth, and the synthesized SAP images. Figure 4.14 has example input images and SAP images from the video. The input frames show the subject we are trying to track as people move in front of him. In the synthetic aperture images, we are able to adjust the focal depth to keep the subject in focus as he moves toward the cameras. The occluding foreground people are blurred away.

At the time when this was filmed, we had only implemented monochrome image warps on the FPGAs. We can now warp color images, too. The performance bottleneck in the system is video decoding and summation on the PC's. Although the cameras can warp

(a)

(b)

Figure 4.14: Live synthetic aperture video. (a) Frames from one of the input cameras, showing the subject to be tracked as people move in front of him. (b) The corresponding synthetic aperture images. We interactively adjust the focal plane to keep the subject in focus as he moves forward.

images at the full 640 x 480 resolution, we configure the MPEG2 encoders to send 320 x 240 I-frame only video to the PCs. At that resolution, the PCs can capture, decode and add 15 monochrome streams each at 30fps. Because the I-frame images are DCT-encoded, we hope to add one more optimization: adding all of frames together in the DCT domain, then applying one IDCT transform to get the final SAP image.

The enhanced contrast example from before hints at the possibilities of digitally improving synthetic aperture photographs. Synthetic aperture video allows even more possibilities for enhancing our data because we can exploit the dynamic nature of the scene. For example, suppose we have for each input image a matte identifying pixels that see through

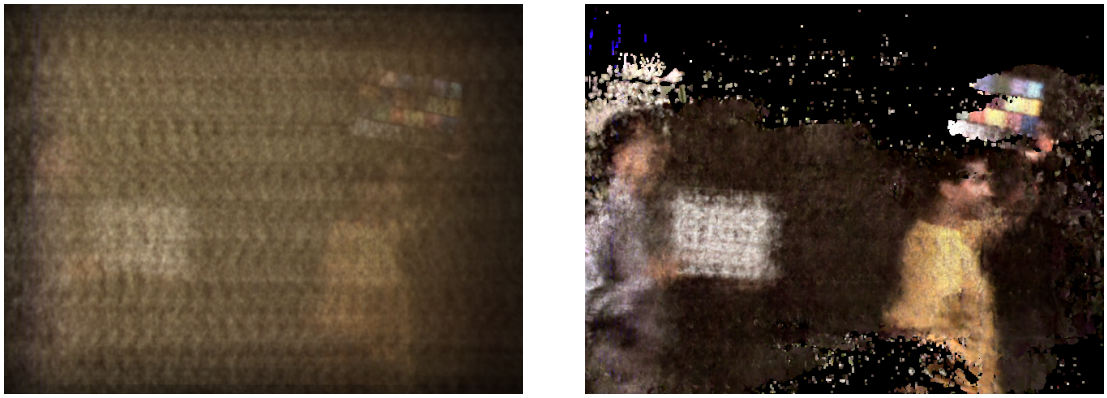

(a) (b)

Figure 4.15: Synthetic aperture with occluder mattes. (a) A regular synthetic aperture image, averaged from all aligned input images. (b) Each pixel in this image is the average of only the corresponding input image pixels that see through the occluder. The contrast is greatly increased because the occluder is eliminated instead of blurred.

the foreground occluder. If instead of averaging pixels from all images to generate the synthetic aperture image, we average only those that see the background, we can eliminate the occluder instead of blurring it away. For a static occluder, there are many ways to generate these mattes. For example, we could place a black surface behind the object, then a white one, and record which pixels change.

Figure 4.15 shows an experiment using another approach—masking all of the pixels which never change during the recorded video. These pixels correspond to the static parts of the video, either the background or the occluder. In practice, we use a threshold so we do not confuse image noise with unoccluded pixels. The image on the left is the usual synthetic aperture image. On the right, each pixel is the average of only the unoccluded pixels in the input images, and the image contrast is much improved. The missing pixels are ones in which no camera saw through the foreground, nothing changed during the video segment, or the changes were below our threshold.

Pixels that contain a mixture of foreground and background colors will corrupt the matted results, and we can expect that our Bayer demosaicing will work poorly for background

colors unless the holes in the occluder are several pixels wide. Color calibration also becomes an issue here. Regular synthetic aperture photography is relatively insensitive to the varying color responses of our sensors. The cameras used to take the images in figure 4.9 were configured identically, but show significant variation. Because the data from all the cameras are averaged together, the differences are averaged away. For the matting experiment, if few values are averaged for a pixel, color variations will have a greater effect. In the next section, we will look at an application with even stricter color calibration requirements: high-speed video capture using a dense camera array.

Chapter 5

Application #2: High-Speed Videography

This chapter explains how we use our camera array as a high-speed video camera by staggering the shutter times of the cameras and interleaving their aligned and color-corrected images. Creating a single high-speed camera from the array requires a combination of fine control over the cameras and compensation for varying geometric and radiometric properties characteristic of cheap image sensors. Interleaving images from different cameras means that uncorrected variations in their radiometric properties will cause frame-to-frame intensity and color differences in the high-speed video. Because the radiometric responses of cheap cameras varies greatly, the cameras in our array must be configured to have relatively similar responses, then calibrated so the remaining differences can be corrected in post-processing.

High-speed videography stresses the temporal accuracy of every imaged pixel, so we must correct for distortions of fast-moving objects due to the electronic rolling shutter in our CMOS image sensors. Rolling shutter images can be thought of as diagonal planes in a spatiotemporal volume, and slicing the volume of rolling shutter images along vertical planes of constant time eliminates the distortions. At the end of the chaptor, I will explore ways to extend performance by taking advantage of the unique features of multiple camera sensors—parallel compression for very long recordings, and exposure windows that span multiple high-speed frame times for increasing the frame rate or signal-to-noise ratio. The

interaction of our geometric alignment with the electronic rolling shutter causes timing errors that can only be partially corrected.

5.1 Previous Work

High-speed imaging has many applications, including analysis of automotive crash tests, golf swings, and explosions. Industrial, research and military applications have motivated the design of faster and faster high-speed cameras. Currently, off-the-shelf cameras from companies like Photron and Vision Research can be found that record 800x600 pixels at 4800fps, or 2.3 gigasamples per second. These devices use a single camera and are typically limited to storing just a few seconds of data because of the huge bandwidths involved in high-speed video. The short recording duration means that acquisition must be synchronized with the event of interest. As we will show, our system lets us stream high-speed video for minutes, eliminating the need for triggers and short recording times by using a parallel architecture for capturing, compressing, and storing high-speed video, i.e. multiple interleaved cameras.

Little work has been done generating high-speed video from multiple cameras running at video frame rates. The prior work closest to ours is that of Shechtman, et al. on increasing the spatiotemporal resolution of video from multiple cameras [48]. They acquire video at regular frame rates with motion blur and aliasing, then synthesize a high-speed video using a regularized deconvolution. Our method, with better timing control and more cameras, eliminates the need for this sophisticated processing, although we will show that we can leverage this work to extend the range of the system.

5.2 High-Speed Videography From Interleaved Exposures

Using n cameras running at a given frame rate s, we create high-speed video with an effective frame rate of $h = n * s$ by staggering the start of each camera's exposure window by $1/h$ and interleaving the captured frames in chronological order. For example, using 52 cameras, we have s=30, n=52, and h=1560fps. Unlike a single camera, we have great flexibility in choosing exposure times. We typically set the exposure time of each camera to be

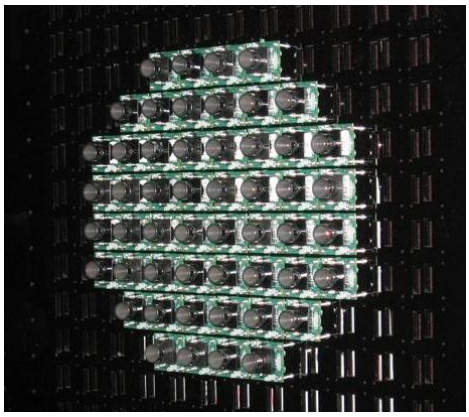

Figure 5.1: An array of 52 cameras for capturing high-speed video. The cameras are packed closely together to approximate a single center of projection.

$1/h$, 650μs in this case, or less. The exposure duration for our Omnivision sensors is programmable in increments of 205μs, corresponding to four row times. Very short exposure times are often light-limited, creating a trade-off between acquiring more light (to improve the signal-to-noise ratio) using longer exposures, and reducing motion blur with shorter exposures. Because we use multiple cameras, we have the option of extending our exposure times past $1/h$ to gather more light and using temporal super-resolution techniques to compute high-speed video. We will return to these ideas later.

Figure 5.1 shows the assembly of 52 cameras used for these experiments. To align images from the different cameras to a single reference view, we make the simplifying assumption that the scene lies within a shallow depth of a single object plane. Under these conditions, we can register images using planar homographies as described in section 4.2. We place the calibration target at the assumed object plane and pick one of the central cameras in the array to be the reference view. Using automatically detected feature correspondences between images, we compute alignment homographies for all other views to the reference view.

Of course, this shallow scene assumption holds only for scenes that are relatively flat or sufficiently distant from the array relative to the camera spacing. Figure 5.2 shows the alignment error as objects stray from the object plane. In this analysis, (although not in our calibration procedure), we assume that our cameras are located on a plane, their optical axes

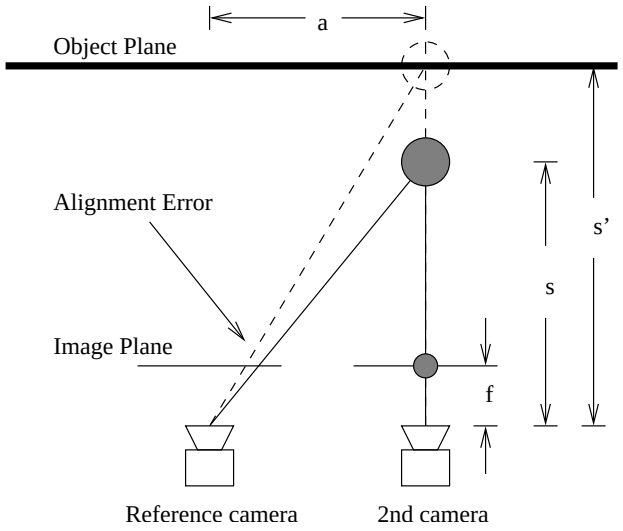

Figure 5.2: Using a projective transform to align our images causes errors for objects off the assumed plane. The solid lines from the gray ball to each camera show where it appears in each view with no errors. The dashed line shows how the alignment incorrectly projects the image of the ball in the second camera to an assumed object plane, making the ball appear to jitter spatially when frames from the two cameras are temporally interleaved.

are perpendicular to that plane, their image plane axes are parallel, and their focal lengths f are the same. For two cameras separated by a distance a, an object at a distance s will see a disparity of $d = fa/s$ between the two images (assuming the standard perspective camera model). Our computed homographies will account for exactly that shift when registering the two views. If the object were actually at distance s' instead of s, then the resulting disparity should be $d' = fa/s'$. The difference between these two disparities is our error (in metric units, not pixels) at the image plane.

Equating the maximum tolerable error c to the difference between d and d', and solving for s' yields the equation

$$s' = \frac{s}{1 - \frac{sc}{fa}}$$

Evaluating this for positive and negative maximum errors gives our near and far effective focal limits. This is the same equation used to calculate the focal depth limits for a pinhole camera with a finite aperture [49]. In this instance, our aperture is the area spanned

Focal Length	Focal Distance	Depth of Field	Hyperfocal Distance
6.0mm	10m	0.82m	242m
	20m	3.3m	
	30m	7.5m	
	100m	99m	
20.0mm	10m	0.24m	809m
	20m	0.99m	
	30m	2.2m	
	100m	25m	

Table 5.1: The effective depth of field for the 52-camera array for different lens focal lengths and object focal distances.

by our camera locations. Rather than becoming blurry, objects off the focal plane remain sharp but appear to move around from frame to frame in the aligned images.

For our lab setup, the object plane is 3m from our cameras, the camera pitch is 33mm, and the maximum separation between any two of the 52 cameras is 251mm. The image sensors have a 6mm focal length and a pixel size of 6.2μm. Choosing a maximum tolerable error of +/- one pixel, we get near and far focal depth limits of 2.963m and 3.036m, respectively, for a total depth of field of 7.3cm.

Note that these numbers are a consequence of filming in a confined laboratory. For many high-speed video applications, the objects of interest are sufficiently far away to allow much higher effective depths of field. To give an idea of how our system would work in such settings, table 5.1 shows how the depth of field grows with object focal depth. It presents two arrangements, the lab setup with 6mm lenses already described, and the same rig with moderately telephoto 20mm lenses. The depth of field grows quickly with distance. For the system with 6mm lenses and an object focal distance of 10m, the depth of field is already nearly a meter. The table also includes the effective hyperfocal distance, h, for the systems. When the object focal depth is set at h, the effective depth of field of the system becomes infinite. The motion in the aligned images of all objects farther than $h/2$ from the camera array will be less than our maximum tolerable error.

The false motion of off-plane objects can be rendered much less visually objectionable by ensuring that sequential cameras in time are spatially adjacent in the camera mount. This

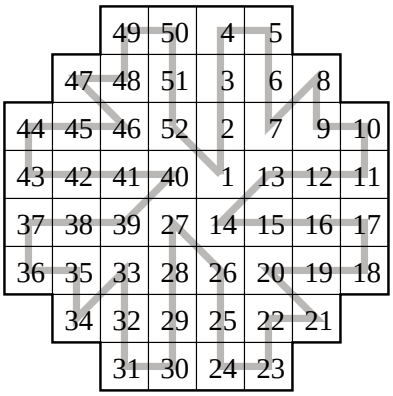

Figure 5.3: The trigger order for our 52 camera array. Ensuring that sequential cameras in the trigger sequence are spatially adjacent in the array makes frame-to-frame false motion of off-plane objects small, continuous and less objectionable.

constrains the maximum distance between cameras from one view in the final high-speed sequence to the next to only 47mm and ensures that the apparent motion of misaligned objects is smooth and continuous. If we allow the alignment error to vary by a maximum of one pixel from one view to the next, our effective depth of field increases to 40cm in our lab setting. Figure 5.3 shows the firing order we use for our 52 camera setup.

5.3 Radiometric Calibration

Because we interleave images from different cameras, uncorrected variations in their radiometric properties will cause frame-to-frame intensity and color differences in the high-speed video. Because the radiometric responses of cheap cameras varies greatly, the cameras in our array must be configured to have relatively similar responses, then calibrated so the remaining differences can be corrected in post-processing.

Color calibration is essential to many view interpolation and high-x algorithms. Light Field Rendering and The Lumigraph, for example, assume that all of the camera images “look alike”—the color and intensity variations between images are due only to the changing camera positions. Furthermore, most computational imaging techniques assume that the camera responses are linear. Even expensive cameras often have nonlinear responses,

so we must also find a way to linearize the sensor response. For a large camera array, these calibration methods must be automatic.

Differences in the response of a camera's pixels to incident illumination from the scene can be due to variations in the sensor's response or to the camera's optics. Here, I summarize these sources of variation, review past efforts to automatically radiometrically calibrate camera arrays, and present methods for automatically configuring and color matching the array.

5.3.1 Camera Radiometric Variations

For a given incident illumination, a camera's image sensor and optics determine its radiometric response. Process variations between sensors (or even between pixels on the same sensor) lead to different responses at each step of the imaging process. The color filters for single-chip color sensors, the photodetectors that collect stray electrons generated by light interacting with silicon, and the circuitry for amplifying and reading out the values sensed at each pixel all contribute to the variations between sensors. The CMOS sensors in our array use "analog processing" for color space conversion and gamma adjustment, adding more sources of variation unless these features are turned off.

The optics on our cameras also cause variations in color response. Cos^4 falloff and vignetting, for example, cause images to get dimmer towards the edges. Less strict manufacturing tolerances for inexpensive lenses also lead to differences in the amount of light they gather. Global differences in the amount of light a lens passes to the sensor are indistinguishable from a global change in the gain of the sensor, so we do not attempt to calibrate our sensor and lenses separately. Furthermore, although intensity falloff is certainly significant for our cameras, we have not yet attempted to calibrate it for our array. Our experience so far has been that it is roughly similar from camera to camera and does not strongly impact our algorithms.

5.3.2 Prior Work in Color Calibrating Large Camera Arrays

Very little work has been done on automatically radiometrically calibrating large camera arrays, most likely because big arrays are still rare. Some systems, such as the 3D-Room,

do not color calibrate their cameras at all, leading to color artifacts [50]. Presumably the automatic gain, offset and white balance controls for their cameras produced acceptable images, even if they varied somewhat between cameras. Yang et al. found that the automatic controls were unreliable for their 64-camera array [15], so they used the method proposed by Nanda and Cutler for an omnidirectional multi-sensor "RingCam" [51].

The RingCam itself was a set of cameras with only partially overlapping views, so the color calibration relies on image statistics in the region of overlap between neighboring cameras. Because this method is the only other one we know of for configuring an array of cameras, I will briefly describe it here before presenting our methods. In the notation of Nanda and Cutler, for a camera with brightness b and contrast c, the relation between an observed pixel value $I(x,y)$ and the accumulated charge $i(x,y)$ on the sensor at that pixel is

$$I(x,y) = b + c * i(x,y)$$

Their image sensors, like ours, have programmable gains (contrasts) and offsets (biases). To configure their cameras, they first set the contrast for their sensors to zero and adjust the offset until the mean image value is some designated "black value." Once the offset has been fixed, they vary the contrast to raise the mean image value to some user-selected level. Finally, they white balance their cameras by filming a white piece of paper and adjusting the red and blue gains of their sensors until the images of the paper have equal red, green and blue components. Their goal was real-time image corrections, so they did not implement any post-processing of the images from their cameras.

Our color calibration goals are different from those of Nanda et al. The RingCam had to deal with highly varying illumination because their cameras had only partially overlapping fields of view and were arranged to cumulatively span a full 360 degrees. For the applications in this thesis, our cameras are usually on a plane and verged to view a common working volume, so the ranges of intensities in the views are more consistent. The RingCam was designed to handle dynamically varying illumination and used blending to mitigate residual color differences between cameras. Our goal is to produce images that require no blending. We fix our camera settings at the start of each acquisition so we can calibrate for a particular setting and post-process the images to correct for variations.

5.3.3 Radiometric Calibration Method

Our calibration method ensures that all cameras view the same range of scene intensities and maximizes the usable data produced in each color channel by all cameras so we can process it later. It is described in detail in Neel Joshi's Master's thesis [8]. We start by configuring all of our cameras to match the same desired linear fit for the gray scale checkers on a Macbeth color checker chart. Our image sensors are highly nonlinear near the top and bottom of their output range, so we fit the response to a line from 20 (out of 255) for the black patch (3.1% reflectance) to 220 for the white patch (90.0% reflectance). We iteratively adjust the programmable green, red and blue gains and offsets on our sensors until the measured responses match the line. Assuming the white patch is the brightest object in our scene, this ensures that we're using the entire range of each color channel and reduces quantization noise in our images. This linear fit has the added benefit of white balancing our cameras.

To ensure that intensity falloff and uneven illumination do not cause errors, we take an image with a photographic gray card in place of the checker chart. With no intensity falloff and uniform illumination, the image of this diffuse gray card would be constant at all pixels. For each camera, we compute scale values for each pixel that correct the nonuniformity and apply them to all image measurements.

Once we have automatically configured the cameras, we apply standard methods to further improve the color uniformity of images. The image sensor response is only roughly linear, so we compute lookup tables to map the slightly nonlinear responses of our cameras to the desired line for the gray scale patches. Then we compute 3x3 correction matrices that we apply to the (R,G,B) pixel values from each camera to generate corrected (R,G,B) values. The matrices minimize the variance between measured values for all of the color checkers in the chart across all of the cameras in the array.

There are a number of ways one could automate this task. We chose to leverage our geometric calibration by attaching the color checker to out geometric calibration target at a fixed location and using homographies to automatically find the locations of the color checker patches. With this method, we can robustly and simply radiometrically configure and calibrate an array of 100 cameras in a matter of minutes.

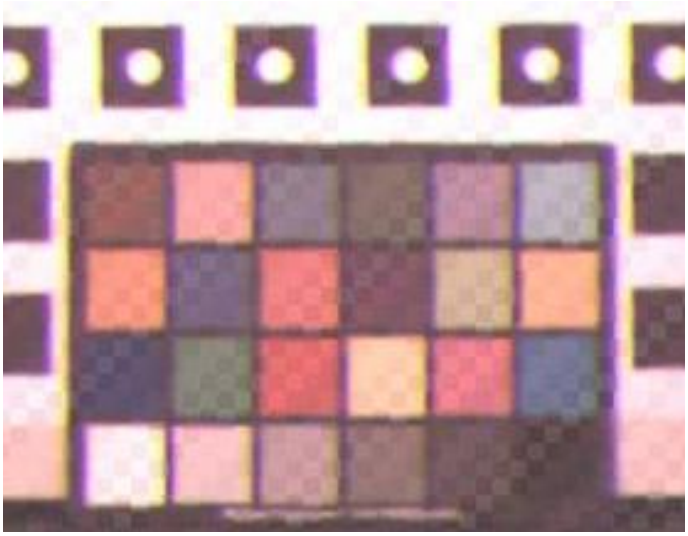

Figure 5.4: A color checker mosaic with no color correction. This image was assembled using 7x7 blocks from different cameras and clearly shows the radiometric variation between them, even though they are configured with identical exposure and color gain settings.

Figure 5.4 shows an image mosaic of a Macbeth color checker chart made with no color calibration. To make this image, we configured all of our cameras with the same gains, took pictures of the target and then applied the planar homography described earlier to warp all the images to one common reference view. We assembled the mosaic from 7x7 pixel blocks from different camera images. Each diagonal line of blocks (diagonal from lower left to upper right) is from the same camera. The color differences are easy to see in this image and give an idea of the process variation between image sensors.

In the figure 5.5 below, we have used our color calibration routines to properly set up the cameras and post-process the images. Note that the color differences are very hard to detect visually. This implies that we should be able to do other types of mosaics and IBR methods for combining images effectively, too. In quantitative terms, the RMS error between color values for any two cameras was 1.7 for red values, 1.0 for green, and 1.4 for blue. The maximum error was larger, 11 for red, 6 for green and 8 for blue. Although the perceptible differences in the resulting images are small, the large maximum errors might cause difficulties for vision algorithms that rely on accurate color information. As we will see in the next chapter, we have successfully use optical flow based vision algorithms on

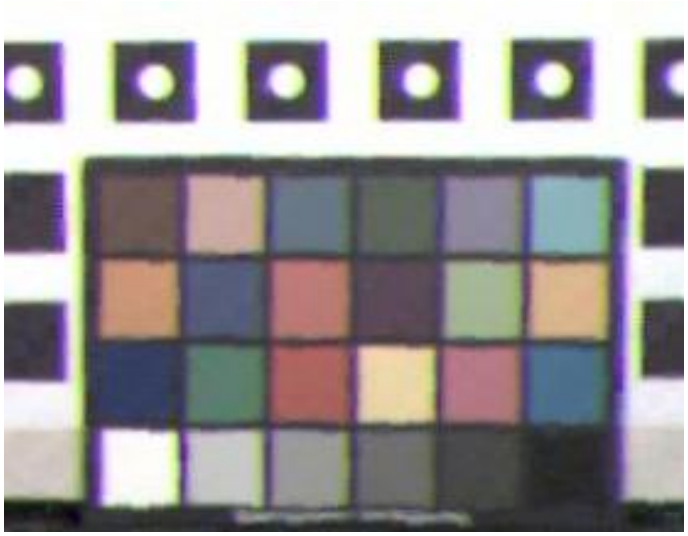

Figure 5.5: A color checker mosaic with color correction. After calibrating our cameras, the color differences are barely discernible.

images from the array to perform view interpolation in space and time.

Our radiometric calibration method has several limitations that might need to be addressed for future applications. The cameras must all see the same calibration target, precluding omnidirectional camera setups like the RingCam. We do not handle dynamically varying illumination, which could be a problem for less controlled settings. Although we take steps to counter intensity falloff in the cameras and nonuniform illumination of our color checker when performing the color calibration, we do not model intensity falloff or try to remove it from our images. Because falloff is similar from camera to camera, and our cameras all share the same viewing volume, the effects are hard to perceive for our applications. For image mosaicing to produce wide field-of-view mosaics, however, this falloff might be very noticeable.

5.4 Overcoming the Electronic Rolling Shutter

For image sensors that have a global, “snapshot” shutter, such as an interline transfer CCD, the high-speed method we have described would be complete. A snapshot shutter starts and

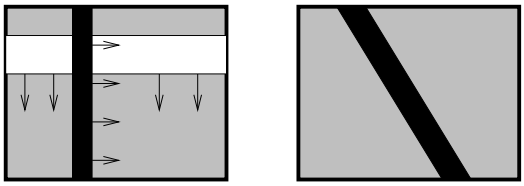

(a) (b)

Figure 5.6: The electronic rolling shutter. Many low-end image sensors use an electronic rolling shutter, analogous to an open slit that scans over the image. Each row integrates light only while the slit passes over it. (a) An example of an object moving rapidly to the right while the rolling shutter scans down the image plane. (b) In the resulting image, the shape of the moving object is distorted.

stops light integration for every pixel in the sensor at the same times. Readout is sequential by scan line, requiring a sample and hold circuit at each pixel to preserve the value from the time integration ends until it can be read out. The electronic rolling shutter in our image sensors, on the other hand, exposes each row just before it is read out. Rolling shutters are attractive because they do not require the extra sample and hold circuitry at each pixel, making the circuit design simpler and increasing the fill factor (the portion of each pixel's area dedicated to collecting light). A quick survey of Omnivision, Micron, Agilent, Hynix and Kodak reveals that all of their color, VGA (640x480) resolution, 30fps CMOS sensors use electronic rolling shutters.

The disadvantage of the rolling shutter, illustrated in figure 5.6, is that it distorts the shape of fast moving objects, much like the focal plane shutter in a 35mm SLR camera. Since scan lines are read out sequentially over the 33ms frame time, pixels lower in the image start and stop integrating incoming light nearly a frame later than pixels from the top of the image.

Figure 5.7 shows how we remove the rolling shutter distortion. The camera triggers are evenly staggered, so at any time they are imaging different regions of the object plane. Instead of interleaving the aligned images, we take scan lines that were captured at the same time by different cameras and stack them into one image.

One way to view this stacking is in terms of a spatiotemporal volume, shown in figure

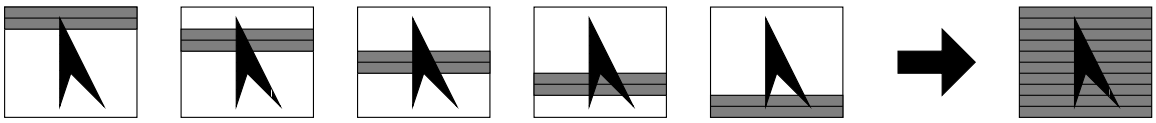

Figure 5.7: Correcting the electronic rolling shutter distortion. The images on the left represent views from five cameras with staggered shutters. At any time, different rows (shown in gray) in each camera are imaging the object plane. By stacking these rows into one image, we create a view with no distortion.

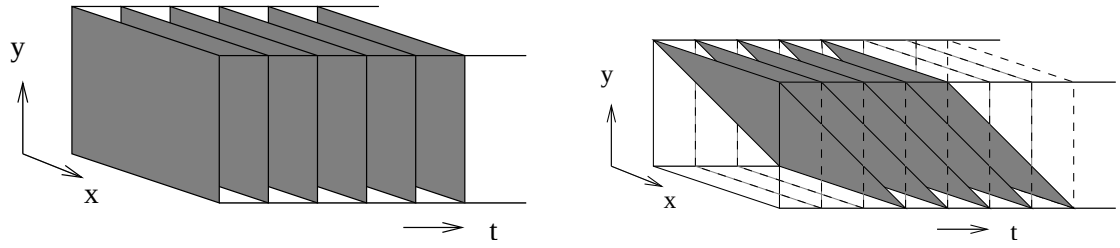

Figure 5.8: Slicing the spatiotemporal volume to correct rolling shutter distortion. (a) Cameras with global shutters capture their entire image at the same time, so each one is a vertical slice in the volume. (b) Cameras with rolling shutters capture lower rows in their images later in time, so each frame lies on a slanted plane in the volume. Slicing rolling shutter video along planes of constant time in the spatiotemporal volume removes the distortion.

5.8. Images from cameras with global shutters are vertical slices (along planes of constant time) of the spatiotemporal volume. Images from rolling shutter cameras, on the other hand, are diagonal slices in the spatiotemporal volume. The scan line stacking we just described is equivalent to slicing the volume of rolling shutter images along planes of constant time. We use trilinear interpolation between frames to create the images. The slicing results in smooth, undistorted images. Figure 5.9 shows a comparison of frames from sliced and unsliced videos of a rotating fan. The videos were filmed with the 52 camera setup, using the trigger ordering in figure 5.3.

The spatiotemporal analysis so far neglects the interaction between the rolling shutter and our image alignments. Vertical components in the alignment transformations raise or

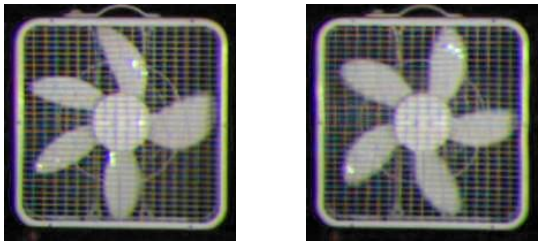

(a) (b)

Figure 5.9: "Slicing" rolling shutter videos to eliminate distortions. (a) An aligned image from one view in the fan sequence. Note the distorted, non-uniform appearance of the fan blades. (b) "Slicing" the stacked, aligned frames so that rows in the final images are acquired at the same time eliminates rolling shutter artifacts. The moving blades are no longer distorted.

lower images in the spatiotemporal volume. As figure 5.10 shows, such displacements also shift rolling shutter images later or earlier in time. By altering the trigger timing of each camera to cancel this displacement, we can restore the desired evenly staggered timing of the images. Another way to think of this is that a vertical alignment shift of x rows implies that features in the object plane are imaged not only x rows lower in the camera's view, but also x row times *later* because of the rolling shutter. A row time is the time it takes the shutter to scan down one row of pixels. Triggering the camera x row times earlier exactly cancels this delay and restores the intended timing. Note that pure horizontal translations of rolling shutter images in the spatiotemporal volume do not alter their timing, but projections that cause scale changes, rotations or keystoning alter the timing in ways that cannot be corrected with only a temporal shift.

We aim our cameras straight forward so their sensors planes are as parallel as possible, making their alignment transformations as close as possible to pure translations. We compute the homographies mapping each camera to the reference view, determine the vertical components of the alignments at the center of the image, and subtract the corresponding time displacements from the cameras' trigger times. As we have noted, variations in the focal lengths and orientations of the cameras prevent the homographies from being strictly translations, causing residual timing errors. In practice, for the regions of interest in our

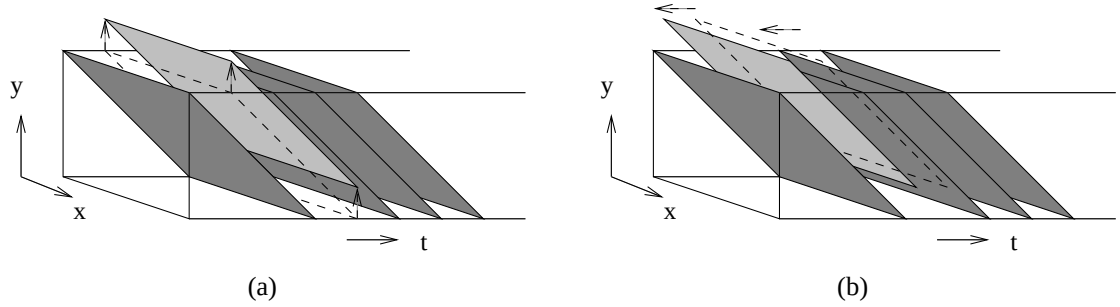

Figure 5.10: Alignment of rolling shutter images in the spatiotemporal volume. (a) Vertically translating rolling shutter images displaces them toward planes occupied by earlier or later frames. This is effectively a temporal offset in the image. (b) Translating the image in time by altering the camera shutter timing corrects the offset. As a result, the image is translated along its original spatiotemporal plane.

videos (usually the center third of the images) the maximum error is typically under two row times. At 1560fps, the frames are twelve row times apart.

The timing offset error by the rolling shutter is much easier to see in a video than in a sequence of still frames. The video fan_even.mpg on the CD-ROM accompanying this thesis shows a fan filmed at 1560fps using our 52 camera setup and evenly staggered trigger times. The fan appears to speed up and slow down, although its real velocity is constant. Note that the effect of the timing offsets is lessened by our sampling order—neighboring cameras have similar alignment transformations, so we do not see radical changes in the temporal offset of each image. Fan_shifted.mpg is the result of shifting the trigger timings to compensate for the alignment translations. The fan's motion is now smooth, but the usual artifacts of the rolling shutter are still evident in the misshapen fan blades. Fan_shifted_sliced.mpg shows how slicing the video from the retimed cameras removes the remaining distortions.

5.5 Results

Filming a rotating fan is easy because no trigger is needed and the fan itself is nearly planar. Now I present a more interesting acquisition: 1560 fps video of balloons popping, several seconds apart. Because our array can stream at high speed, we did not need to explicitly

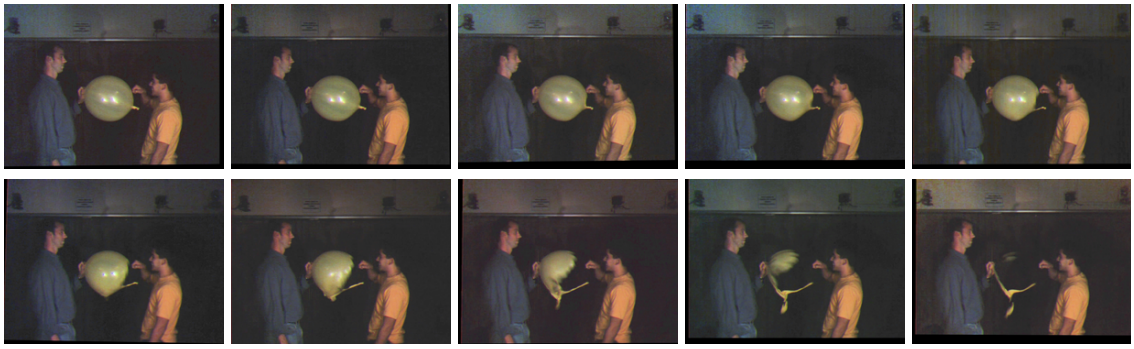

Figure 5.11: 1560fps video of a popping balloon with rolling shutter distortions. The balloon is struck at the top by the tack, but it appears to pop from the bottom. The top of the balloon seems to disappear.

synchronize video capture with the popping of the balloons. In fact, when we filmed we let the video capture run while we walked into the center of the room, popped two balloons one at a time, and then walked back to turn off the recording. This video is also more colorful than the fan sequence, thereby exercising our color calibration.

Figure 5.11 shows frames of one of the balloons popping. We have aligned the images but not yet sliced them to correct rolling shutter-induced distortion. This sequence makes the rolling shutter distortion evident. Although we strike the top of the balloon with a tack, it appears to pop from the bottom. These images are from the accompanying video balloon1_distorted.mpg. In the video, one can also see the artificial motion of our shoulders, which are in front of the object focal plane. Because of our camera ordering and tight packing, this motion, although incorrect, is relatively unobjectionable. Objects on the wall in the background, however, are much further from the focal plane and exhibit more motion.

Figure 5.12 compares unsliced and sliced images of the second balloon in the sequence popping. These sliced frames are from balloon2_sliced.mpg. In the unsliced sequence, the balloon appears to pop from several places at once, and pieces of it simply vanish. After resampling the image data, the balloon correctly appears to pop from where it is punctured by the pin. This slicing fixes the rolling shutter distortions but reveals limitations of our approach: alignment errors and color variations are much more objectionable in the sliced video. Before slicing, the alignment error for objects off the focal plane was constant for a

given depth and varied somewhat smoothly from frame to frame. After slicing, off-plane objects, especially the background, appear distorted because their alignment error varies with their vertical position in the image. This distortion pattern scrolls down the image as the video plays and becomes more obvious. Before slicing, the color variation of each camera was also confined to a single image in the final high-speed sequence. These short-lived variations were then averaged by our eyes over several frames. Once we slice the images, the color offsets of the images also create a sliding pattern in the video. Note that some color variations, especially for specular objects, are unavoidable for a multi-camera system.The reader is once again encouraged to view the videos on the companion CD to appreciate these effects. The unsliced video of the second balloon popping, balloon2_distorted.mpg, is included for comparison, as well as a continuous video showing both balloons, balloons.mpg.

The method presented acquires very high-speed video using a densely packed array of lower frame rate cameras with precisely timed exposure windows. The parallel capture and compression architecture of the array lets us stream essentially indefinitely. The system scales to higher frames rates by simply adding more cameras. Inaccuracies correcting the the temporal offset caused by aligning our rolling shutter images are roughly one sixth of our frame time and limit the scalability of our array. A more fundamental limit to the scalability of the system is the minimum integration time of the camera. At 1560fps capture, the exposure time for our cameras is three times the minimum value. If we scale beyond three times the current frame rate, the exposure windows of the cameras will begin to overlap, and our temporal resolution will no longer match our frame rate.

The possibility of overlapping exposure intervals is a unique feature of our system—no single camera can expose for longer than the time between frames. If we can use temporal super-resolution techniques to recover high-speed images from cameras with overlapping exposures, we could scale the frame rate even higher than the inverse of the minimum exposure time. As exposure times decrease at very high frame rates, image sensors become light limited. Typically, high-speed cameras solve this by increasing the size of their pixels and using very bright lights. Applying temporal super-resolution overlapped high-speed exposures is another possible way to increase the signal-to-noise ratio of a high-speed multi-camera system. To see if these ideas show promise, I applied the temporal super-resolution

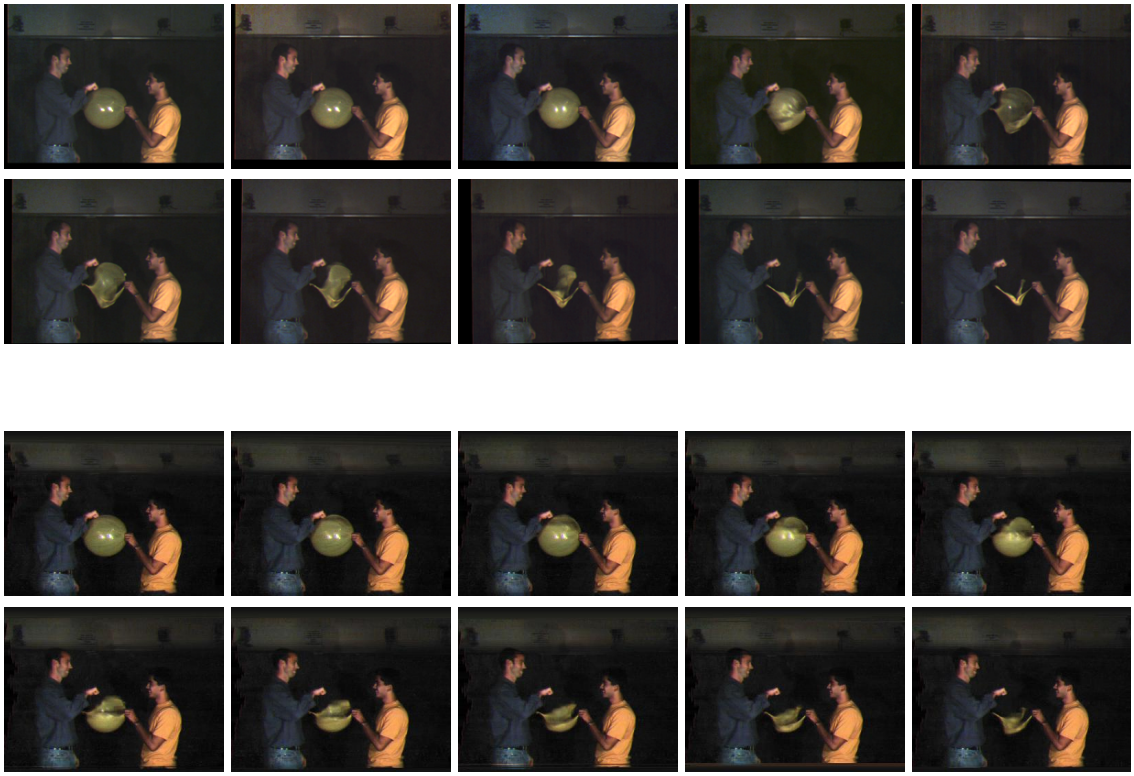

Figure 5.12: Comparison of the sliced and unsliced 1560fps balloon pop. The top set of ten pictures are interleaved rolling shutter images. The balloon appears to pop from several places at once, and pieces of it disappear. Properly resampling the volume of images produces the lower set of ten images, revealing the true shape of the popping balloon.

method presented by Shechtman [48] to video of a fan filmed with an exposure window that spanned four high-speed frame times. The temporal alignment process was omitted because the convolution that relates high-speed frames to our blurred images is known. Figure 5.13 shows a comparison between the blurred blade, the results of the temporal super-resolution, and the blade captured in the same lighting with a one frame exposure window. Encouragingly, the deblurred image becomes sharper and less noisy.

There are several opportunities for improving this work. One is a more sophisticated alignment method that did not suffer from artificial motion jitter for objects off our assumed focal plane. Another is combining the high-speed method with other multiple camera applications. In the next chapter, I will discuss an application that does both–spatiotemporal

v

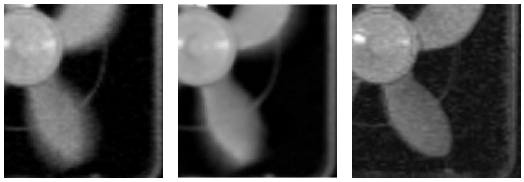

(a) (b) (c)

Figure 5.13: Overlapped exposures with temporal super-resolution. (a) Fan blades filmed with an exposure window four high-speed frames long. (b) Temporal super-resolution yields a sharper, less noisy image. Note that sharp features like the specular highlights and stationary edges are preserved. (c) A contrast enhanced image of the fan filmed under the same lighting with an exposure window one fourth as long. Note the highly noisy image.

view interpolation.

Chapter 6

Application #3: Spatiotemporal View Interpolation

The synthetic aperture and high-speed videography applications presented in the last two chapters use an array of cameras, accurate calibration, and precise camera control to enhance performance along a single metric. Nothing prevents us from using this set of tools to simultaneously improve multiple aspects of camera performance. For example, we could create a high-speed, synthetic aperture video camera using staggered sets of synchronized cameras spread across the synthetic aperture. Another possibility would be a high dynamic range, high-resolution video camera constructed from camera clusters, where the cameras in each cluster have the same field of view but varying exposure times, and their fields of view abut.

This chapter explores using a dense array of cameras with staggered trigger times to increase our sampling resolution in both space and time for spatiotemporal view interpolation. We look at the more general problem of optimal sampling patterns and interpolation methods for the spatiotemporal volume of images that the camera array records. Large video camera arrays are typically synchronized, but we show that staggering camera triggers provides a much richer set of samples on which to base the interpolation. Richer sampling not only improves the simplest interpolation methods, blending and nearest neighbor, but also lets one interpolate new space-time views using simple, robust, image-based methods with simple calibration. We present a novel optical flow method that combines a plane

plus parallax framework with knowledge of camera spatial and temporal offsets to generate flow fields for virtual images at new space-time locations. We present results interpolating video from a 96-camera light field.

6.1 Introduction

Spatiotemporal view interpolation is the creation of new scene views from locations and times different from those in the captured set of images. The simplest spatiotemporal interpolation method is extending light field rendering to video by linearly interpolating in time. For this reconstruction to work, the image volume must be band-limited. Such prefiltering adds undesirable blur to the reconstructed images. Even with very large camera arrays, the sampling density is not sufficiently high to make the blur imperceptible. If the images are not band-limited, the output exhibits ghosting artifacts. This occurs for large disparities or temporal motions.

To avoid the conflicting requirements for sharp images with no sampling artifacts, most image based rendering systems use more sophisticated interpolation schemes based on an underlying scene model. The simplest method is to estimate motion in an image based on local information from neighboring views. Other methods generate increasingly sophisticated three-dimensional models of the scene. Motion estimation grows less robust as the "distance" between camera images increases. More complicated models can handle more widely separated images, but their runtime increases as more global information is incorporated.

The temporal sampling strategy for an array of cameras–when each camera triggers–affects reconstruction. Traditionally, designers of camera arrays have striven to synchronize their cameras. This often leads to much more temporal motion between camera frames than parallax motion between neighboring cameras. Instead, staggered triggers are a better sampling strategy. Improved temporal sampling decreases temporal image motion, allowing us to use simpler, more robust interpolation methods such as optical flow. I will present a spatiotemporal view interpolation method that uses plane + parallax calibration to factor optical flow into parallax and temporal motion components between multiple camera views.

The next section describes previous work in capturing and interpolating between space-time image samples. I'll review plane + parallax geometry and our rendering methods, then describe a framework for determining how best to distribute our camera array samples in time. Even for basic linear or nearest neighbor, better sampling greatly improves reconstruction. Finally, I will describe a method for determining spatial and temporal motion between several views in space and time using optical flow.

6.2 Previous Work

We have already discussed prior work in camera array design and spatial view interpolation. The Manex Entertainment "Bullet Time" system simulated a physically impossible space-time camera trajectory through a dynamic scene, but the path must be specified in advance. The cameras capture the views needed for a single camera path. The goal of the work in this chapter is to investigate how well one could do "Bullet Time" effects as a post-processing step for a captured set of images without specifying the view trajectory in advance.

Spatiotemporal view interpolation depends on sampling strategies and interpolation methods. Lin and Shum [52] present a maximum camera spacing for static light fields with a constant depth assumption, and Chai et al. [53] analyze the minimum spatial sampling rate for static light fields including geometry information. Neither of these works address temporal sampling rates for video light fields. Vedula et al. [54] and Carceroni and Kutulakos [55] present methods for interpolating new space-time views using arrays of synchronized cameras with coincident triggers. They explicitly solve for scene reflectance, structure and motion. By contrast, my system exploits large numbers of inexpensive sensors and improved temporal sampling to reduce spatiotemporal view interpolation to a simpler, image-based task.

6.3 Calibration and Rendering

For this work, the cameras are assembled either in a line or a plane so we can take advantage of plane + parallax calibration. Because this calibration is central to this work, I will briefly review it. Starting with a planar array of cameras, we align all of the camera images to

a fronto-parallel reference plane using 2D image homographies. In the aligned images, points in the scene lying on the reference plane show no parallax between views. Points off the reference plane will have a parallax of $\Delta p = \Delta x \cdot d$, where Δx is the vector from C_0 to C_1 in the camera plane, and d is the relative depth of the point. This has two implications:

- Once we have aligned images to a common reference plane, the parallax between aligned images of a single point off the reference plane is enough to determine the relative locations in the camera plane of all of the cameras. As shown by Vaish et al. [7], the camera displacements can be computed robustly from multiple measurements using a rank-1 factorization via SVD.

- Given the relative camera displacements in the camera plane, the relative depth of a point in one view suffices to predict its location in all other views. This provides a powerful way to combine data from many images.

Once again, we will align all of our input images to a reference plane. The aligned images provide a common space in which to analyze and combine views. Levoy and Hanrahan represent light fields with a two-plane (u,v,s,t) parametrization. For a planar array of cameras, the aligned images correspond (s,t) parameterized images for light field rendering, so measuring motion in the reference plane indicates how much aliasing we would see in reconstructed light field images. We will use this framework both to analyze temporal sampling requirements and for determining image flow between neighboring space-time views.

Aligning our images to a reference plane automatically corrects for geometric variations in our cameras (excluding translations out of the camera plane and radial distortion, which we have found to be negligible for our application). The aligned images are generally off-axis projections, which are visually disturbing. This is clear from the aligned views of the calibration target in figure 4.7–the reference plane will always appear fronto-parallel, regardless of the camera position.

The transformation that we need for rendering corrects the off-axis projection and is equivalent to taking a picture of the aligned plane from the virtual camera position. Plane + parallax calibration does not provide enough information to do this. If we fix the relative

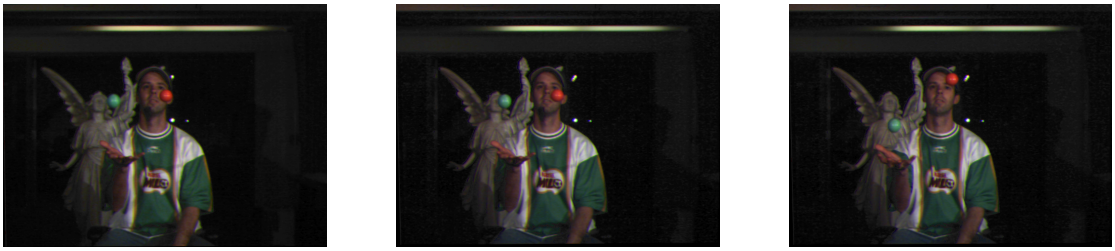

(a) (b) (c)

Figure 6.1: For synchronized cameras, the motion due to parallax between neighboring cameras is often much less than the temporal motion between frames for the same camera. (a) and (b) are images from adjacent cameras at the same point in time. Disparities between images are small. (c) shows a picture from the same camera as (b), one frame later. The motion is obvious and much larger.

camera locations produced by our calibration, the missing information corresponds to the field of view of our reference camera and the distance from the camera plane to the reference plane. These quantities can be determined either by calibrating the reference camera relative to the reference plane or simple manual measurement. In practice, we have found that small errors in these quantities produce very subtle perspective errors and are visually negligible.

6.4 Spatiotemporal Sampling

We now turn our attention to the temporal distribution of our samples. We assume that our cameras all run at a single standard video rate (30fps for our array), that they are placed on a planar grid, and that the desired camera spacing has already been determined. Figure 6.1 shows aligned synchronized images from our array of 30fps video cameras. Differences between images are due to two components: parallax between views and temporal motion between frames. From the images, it is clear that the temporal image motion is much greater than the parallax for neighboring views in space and time. This suggests that we should sample more finely temporally to minimize the maximum image motion between neighboring views in space and time. In the next section, we show how temporal and spatial

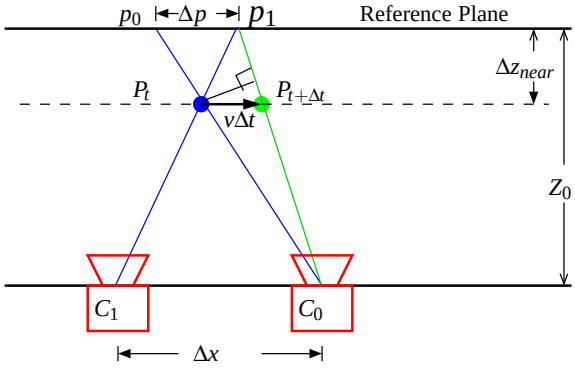

Figure 6.2: The temporal and spatial view axes are related by image motion. For a given scene configuration, we can determine a time step Δt for which the maximum image motion between temporal samples is equal to the maximum parallax between spatially neighboring views. If we measure time in increments of Δt and space in increments of the camera spacing, then the Manhattan distance between (x,y,t) view coordinates corresponds to the maximum possible image motion between views.

view sampling are related by image motion.

6.4.1 Normalizing the Spatial and Temporal Sampling Axes

For a given location of the reference plane at a distance Z_0 from the camera plane, if we bound the maximum parallax in our aligned images, we can establish near and far depth limits for our scene, z_{near} and z_{far}. Alternatively, we could determine the minimum and maximum depth limits of our scene and place the reference plane accordingly [53]. The near and far bounds and camera spacing Δx determine the maximum parallax for any point between neighboring cameras. Given this near depth limit z_{near} and a maximum velocity of v for any object in the scene, we can determine the time for which the maximum possible temporal image motion equals the maximum parallax between neighboring views. This is shown in figure 6.2. The temporal motion for P in camera C_0 is greatest if it is at the near depth limit and moves such that the vector P_tP_{t+1} is orthogonal to the projection ray from C_0 at time $t+1$. If we assume a narrow field of view for our lenses, we can approximate this with a vector perpendicular to the reference plane, shown as $v\Delta t$. If P has velocity v, the maximum temporal motion of its image in C_0 is $\frac{v\Delta t Z_0}{Z_0 - \Delta Z_{near}}$. Equating this motion to the

maximum parallax for P in a neighboring camera yields

$$\Delta t = \frac{\Delta X Z_{near}}{v \Delta Z_0} \tag{6.1}$$

This is the time step for which maximum image motion equals maximum parallax between neighboring views.

Measuring time in increments of the time step Δt and space in units of camera spacings provides a normalized set of axes to relate space-time views. A view is represented by coordinates (x, y, t) in this system. For nearest-neighbor or weighted interpolation between views, measuring the Manhattan distance between view positions in these coordinates will minimize jitter or ghosting during reconstruction. We use Manhattan instead of euclidean distance because the temporal and parallax motions could be parallel and in the same direction. Choosing a temporal sampling period equal to Δt will ensure that maximum temporal motion between frames will not exceed the maximum parallax between neighboring views.

Determining maximum scene velocities ahead of time (for example, from the biomechanics of human motion, or physical constraints such as acceleration due to gravity) can be difficult. An alternative to computing the motion is filming a representative scene with synchronized cameras and setting the time step equal to the ratio between the maximum temporal and parallax motions for neighboring views. One could even design a camera array that adaptively determined the time step based on tracked feature points between views.

6.4.2 Spatiotemporal Sampling Using Staggered Triggers

The time step Δt tells us the maximum temporal sampling period that will ensure temporal resolution at least as good as the spatial resolution across views. One could increase the temporal sampling rate by using an array of high-speed cameras, but this could be prohibitively expensive and would increase demands on data bandwidth, processing, and storage. By staggering the cameras' trigger times, we can increase the temporal sampling rate without adding new samples.

Our goal is to ensure even sampling in space and time using our normalized axes. A convenient way to do this is with a tiled pattern, using the minimum number of evenly

6	1	4
3	0	7
8	5	2

Figure 6.3: An example trigger pattern for a 3x3 array of cameras with nine evenly staggered triggers. The numbers represent the order in which cameras fire. The order was selected to have even sampling in the (x,y,t) space across the pattern. We tessellate larger arrays with patterns such as this one to ensure even spatiotemporal sampling.

staggered trigger times that gives an offset less than Δt. To approximate uniform sampling, the offsets are distributed evenly within the tile, and the pattern is then replicated across the camera array. Figure 6.3 shows an example trigger pattern for a 3x3 array of cameras. For larger arrays, this pattern is replicated vertically and horizontally. The pattern can be truncated at the edges of arrays with dimensions that are not multiples of three.

We used the tiled sampling pattern for our experiments because they were convenient and we had an approximation of the maximum scene velocity. For general scene sampling, especially with unknown depth and velocity limits, these patterns are not optimal. When filming scenes with high temporal image velocities, no two cameras should trigger at the same time. Instead, the trigger times should be evenly distributed across the 30Hz frame time, as in the high-speed video method, to provide the best temporal sampling resolution. For scenes with low velocities, parallax image motion dominates over temporal motion, so we must still ensure even temporal sampling within any local window. Thus, in the general case, the sampling must be temporally uniform over any size spatial region of cameras. One way to accomplish this might be to replicate and gradually skew a local trigger pattern across the entire array.

6.5 Interpolating New Views

We can now create our distance measure for interpolation. The plane + parallax calibration gives up camera positions in the camera plane up to some scale factor. We normalize these positions by dividing by the average space between adjacent cameras, so the distance from

a camera to its horizontal and vertical neighbors is approximately one. Let (x,y) be the position of each camera in these normalized coordinates, and let t be the time at which a given image is acquired, measured in time steps of Δt. Because we have chosen a time step that sets the maximum parallax between views equal to the maximum temporal motion between time steps, the euclidean distance between the (x,y,t) coordinates representing two views is a valid measure of the maximum possible motion between the two images.

The simplest way we could interpolate new views would be to use nearest neighbors as in the high-speed videography method of chapter 5. This method produces acceptable results, but as points move off the reference plane, their images jitter due to parallax between views. The perceived jitter can be reduced using interpolation between several nearby views. To determine which images to blend and how to weight them, we compute a Delauney tessellation of our captured image coordinates. For a new view (x,y,t), we find the tetrahedron of images in the tessellation containing the view and blend the images at its vertices using their barycentric coordinates as weights. Using this tessellation and barycentric weighting ensures that our blending varies smoothly as we move the virtual viewpoint. As we leave one tetrahedron, the weights of dropped vertices go to zero. Our temporal sampling pattern is periodic in time, so we only need to compute the tessellation for three 30Hz sampling periods to compute the weights for an arbitrarily long sequence.

Figure 6.4 shows the benefits of improved temporal sampling. In this experiment, we used a 12x8 array of 30fps video cameras similar to that shown in figure 3.4 to film me heading a soccer ball. The cameras were triggered according to the pattern in figure 6.3, tiled across the array. We then generated 270fps interpolated video using several methods. First, we used a cross-dissolve between sequential frames at one camera to simulate linear interpolation for a synchronized array. The motion of the soccer ball between captured frames is completely absent. Next, we used nearest-neighbor interpolation, which assembles a video sequence using video captured at the proper time from neighboring cameras. This produces sharp images and captures the path of the ball, but the motion is jittered due to parallax between views. Finally, we used the barycentric weighted averaging described previously. This reduces the ball's motion jitter but introduces ghosting.

Staggering the cameras clearly improves our temporal resolution and results in much better results even for simple nearest-neighbor and weighted interpolation. Because our

(a) (b) (c)

Figure 6.4: Better temporal sampling improves interpolation. (a) Linear interpolation between frames in time for a synchronized camera array is just a cross-dissolve. (b) Nearest-neighbor interpolation using staggered cameras produces sharp images, but this composite of multiple images shows that the path of the ball is jittered due to parallax between different cameras. (c) Weighted interpolation using the nearest views in time and space reduces the perceived jitter but causes ghost images.

input images are not band-limited in space and time, new views interpolated with either of these methods will always suffer from artifacts if the motion between views in time or space is too great. One could imagine prefiltering spatially as described in [5], or temporally by using overlapped exposure windows, but prefiltering adds undesirable blur to our images. In the next section, we improve our space-time view interpolation by analyzing the motion between captured images.

6.6 Multi-baseline Spatiotemporal Optical Flow

We have seen that distributing samples from a dense camera array more evenly in time improves spatiotemporal view interpolation using nearest-neighbor or weighted interpolation. Reducing the image motion between captured spatiotemporal views can also decrease the complexity or increase the robustness of other interpolation methods. The combination of dense cameras, improved temporal sampling, and plane + parallax calibration allows one to compute new views robustly using optical flow. We call this “multi-baseline spatiotemporal optical flow” because it computes flow using data from multiple images at different spatial and temporal displacements (also known and baselines).

We extended Black and Anandan's optical flow method [56] using code available on the author's web site. Their algorithm is known to handle violations of the intensity constancy and smoothness assumptions well using robust estimation. It uses a standard hierarchical framework to capture large image motions, but can fail due to masking when small regions of the scene move very differently from a dominant background [57]. For our 30fps synchronized juggling sequence, the algorithm succeeded between cameras at the same time but failed between subsequent frames from the same camera. The motion of the small juggled balls was masked by the stationary background. Once we retimed the cameras, the motion of the balls was greatly reduced, and the algorithm computed flow accurately between pairs of images captured at neighboring locations and time steps.

Our modified spatiotemporal optical flow algorithm has two novel features. First, we solve for a flow field at the (x,y,t) location of our desired virtual view. This was inspired by the bidirectional flow of Kang et al. [58], who observe that for view interpolation, computing the flow at the new view position instead of either source image handles degenerate flow cases better and avoids the hole-filling problems of forward-warping when creating new views. They use this to compute flow at a frame halfway between two images in a video sequence. Typically, optical flow methods will compute flow between two images by iteratively warping one towards the other. They calculate flow at the halfway point between two frames by assuming symmetric flow and iteratively warping both images to the midpoint. We extend the method to compute flow at a desired view in our normalized (x,y,t) view space. We iteratively warp the nearest four captured images toward the virtual view and minimize the weighted sum of the robust pairwise data errors and a robust smoothness error.

Motion cannot be modeled consistently for four images at different space-time locations using just horizontal and vertical image flow. The second component of this algorithm is simultaneously accounting for parallax and temporal motion. We decompose optical flow into the traditional two-dimensional temporal flow plus a third flow term for relative depth that accounts for parallax between views. The standard intensity constancy equation for optical flow is

$$I(i,j,t) = I(i+u\delta t, j+v\delta t, t+\delta t) \tag{6.2}$$

Here, (i, j, t) represent the pixel image coordinates and time, and u and v are the horizontal and vertical motion at an image point. We use i and j in place of the usual x and y to avoid confusion with our view coordinates (x, y, t).

Plane + parallax calibration produces the relative displacements of all of our cameras, and we know that parallax between two views is the product of their displacement and the point's relative depth. Our modified intensity constancy equation includes new terms to handle parallax. It represents constancy between a desired virtual view and a nearby captured image at some offset $(d\delta x, d\delta y, d\delta t)$ in the space of source images. It accounts for the relative depth, d, at each pixel as well as the temporal flow (u, v):

$$I_{virtual}(i, j, x, y, t) = I_{source}(i + u\delta t + d\delta x, j + v\delta t + d\delta y, t + \delta t) \tag{6.3}$$

This equation can be solved for each pixel using a modification of Black's robust optical flow. Appendix A describes the implementation details.

We compute flow using four images from the tetrahedron which encloses the desired view in the same Delauney triangulation as before. The images are progressively warped toward the common virtual view at each iteration of the algorithm. We cannot test the intensity constancy equation for each warped image against a virtual view, so we instead minimize the error between the four warped images themselves, using the sum of the pair-wise robust intensity constancy error estimators. This produces a single flow map, which can be used to warp the four source images to the virtual view. We currently do not reason about occlusions and simply blend the flowed images using their barycentric weights in the tetrahedron.

Figure 6.5 compares view interpolation results using our spatiotemporal optical flow versus a weighted average. Because the computed flow is consistent for the four views, when the source images are warped and blended, the ball appears sharp. The st_interp1.mp4 video on the companion CD-ROM compares blending, nearest neighbor and flow-based interpolation for this dataset. The sequences in which the viewpoint is fixed show that the flow-based interpolation is exactly the registration required to remove alignment errors in the high-speed video method of the previous chapter.

To allow a greater range of virtual camera movement, we configured our cameras in a

(a) (b)

Figure 6.5: View interpolation using space-time optical flow. (a) Interpolated 270fps video using weighted average of four source images. (b) Interpolated 270fps video using optical flow. The four source images were warped according to the computed flow and then averaged using the same weights as in image a. No double images are present because parallax and motion for the ball were correctly recovered.

30 wide by 3 tall array. We used the same 3x3 trigger ordering, tiled across the array. In st_interp2.mp4 on the CD-ROM, we show another soccer sequence in which we alternate smoothly between rendering from one view position at 270fps to freezing time and rendering from novel viewing positions. Figure 6.6 shows twenty frames with a slowly varying viewing positions and times. Figure 6.7 shows five frames spanning the spatial viewing range of the array.

6.7 Discussion

Our multiple camera array allows us to control the image samples that are recorded from the spatiotemporal volume a scene generates, and the sampling pattern chosen greatly affects the complexity of the view interpolation task. While in theory it is possible to simply resample a linear filtered version of the samples to generate new views, even with large numbers of inexpensive cameras, it seems unlikely one could obtain high enough sampling density to prevent either blurred images or ghosting artifacts. Instead, the correct placement

of samples allows the use of simpler modeling approaches rather than none at all. The key question is, how sophisticated a model is needed and what sampling basis allows the most robust modeling methods to be used to construct a desired view?

For many interpolation methods, minimizing image motion leads to better quality view synthesis, so we use minimizing image motion to guide our sample placement. Given our relatively planar camera array, we use a very simple plane + parallax calibration for interpolation in space. For images aligned to a reference plane, spatial view motion results in parallax for points not on the reference plane. This motion must be balanced against temporal image motion. In our camera array this disparity motion is modest between adjacent cameras, and is much smaller than the true motion from frame to frame.

Staggering camera trigger in time distributes samples to reduce temporal image motion between neighboring views without adding new samples. In a way staggered time sampling is never a bad sampling strategy. Clearly the denser time samples help for scenes with high image motion. For scenes with small motion, the denser time samples do no harm. Since the true image motion is small, it is easy to estimate the image at any intermediate time, undoing the time skew adds little error. Since the spatial sampling density remains unchanged, it does not change the view interpolation problem at all. Better temporal sampling lets us apply relatively simple, fairly robust models like optical flow to view interpolation in time and space. We solve for temporal image motion and image motion due to parallax which improves our interpolation.

Because our flow-based view interpolation methods are local, the constraints on the camera timings are also local. They need to sample evenly in every local neighborhood. We use a simple tessellated pattern with locally uniform sampling at the interior and across boundaries. Algorithms that aggregate data from an entire array of cameras will benefit from different time stagger patterns and raises the interesting question of finding an optimal sampling pattern for a few of the more sophisticated model-based methods.

While it is tempting to construct ordered dither patterns to generate unique trigger times for all cameras there is a tension between staggered shutters to increase temporal resolution and models that exploit the rigid-body nature of a single time slice. This seems to be an exciting area for further research.

Staggered trigger times for camera arrays increase temporal resolution with no extra

cost in hardware or bandwidth, but have other limits. One fundamental limit is the number of photons imaged by the cameras if the exposure windows are non-overlapping. The aperture time for each camera is set to be equal to the smallest time difference between the cameras. While this minimizes unintended motion blur, allowing sharp images in "Bullet time" camera motion, at some point the number of photons in the scene will be too small, and the resulting image signal to noise ratio will begin to increase. This gives rise to another dimension that needs to be explored—optimizing the relation between the minimum spacing between time samples and the aperture of the cameras. As mentioned earlier, Shechtman et al. [48] have done some promising work in this area, using multiple unsynchronized cameras with overlapping exposures to eliminate motion blur and motion aliasing in a video sequence.

For our image-based methods, uniform spatiotemporal sampling limits image motion and enhances the performance of our interpolation methods. We analyzed spatiotemporal sampling from the perspective of interpolation with a constant depth assumption and related the temporal and spatial axes with maximum image motions due to parallax and time. That constant-depth assumption is one of the limitations of this work. In the future, I would like to enable more general scene geometries. The spatiotemporal optical flow method generates significantly better results than weighted averaging, but still suffers from the standard vulnerabilities of optical flow, especially occlusions and masking.

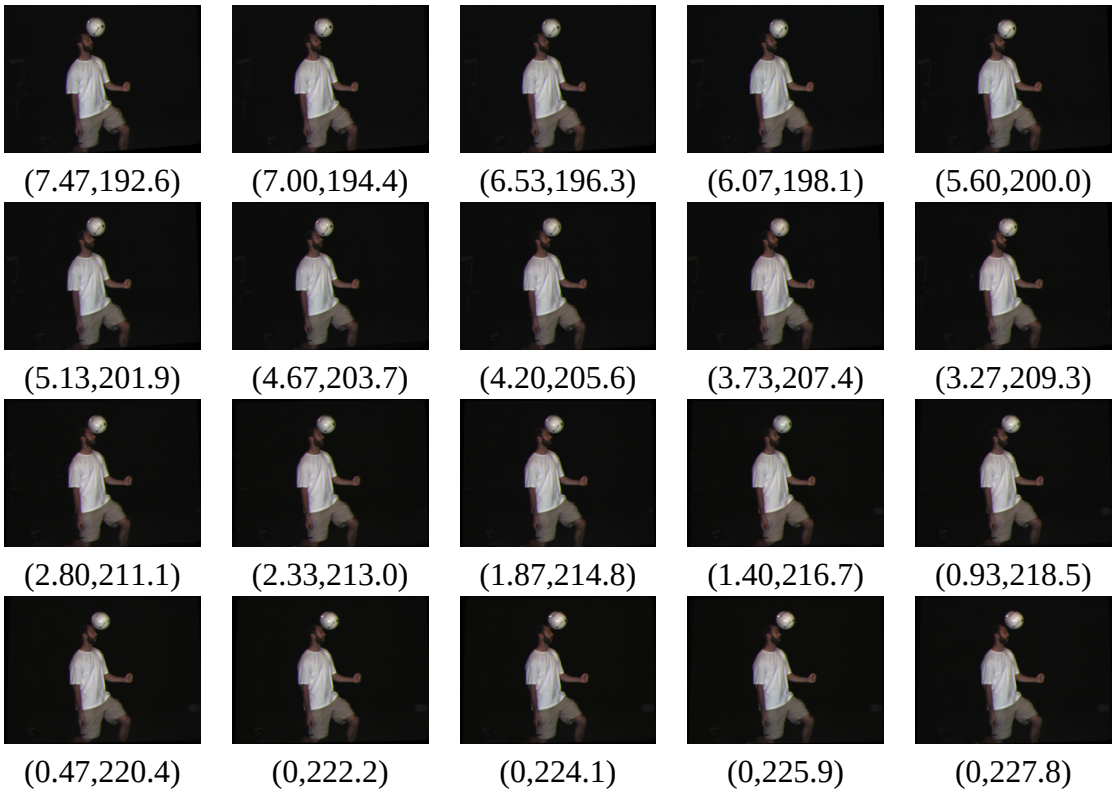

Figure 6.6: Twenty sequential frames from an interpolated video sequence demonstrating slowly varying view positions and times. The input data were captured using a 30x3 array of cameras with nine different trigger times. All views shown are synthesized. Beneath each image are the (x,t) view coordinates, with x in units of average camera spacings (roughly three inches) and t in milliseconds. Motion is more evident looking across rows or along diagonals from top left to bottom right.

Figure 6.7: Five synthesized views showing the spatial viewing range for the 30x3 configuration. View spatial coordinate is again in units of camera spacings, roughly three inches.

Chapter 7

Conclusions

Digital video cameras are becoming cheap and widespread, creating new opportunities for increased imaging performance. Researchers in this space encounter several obstacles. For system designers, large video camera arrays generate data at rates that overwhelm commodity personal computers and storage media. Inexpensive commodity cameras do not offer the degree of control or flexibility required for research. Assuming some system for collecting data from many cameras, researchers must devise calibration methods that scale to large numbers of cameras, and vision and graphics algorithms that robustly account for the lower image quality and more varied geometric and radiometric properties of inexpensive camera arrays.

The architecture in this thesis addresses the issues of scale in large camera array design. It exploits CMOS image sensors, IEEE1394 communication and MPEG video compression to control and capture video from very large numbers of cameras to a few PCs. A flexible mounting system lets us explore many different configurations and applications. I have shown three applications demonstrating that we can effectively combine data from many inexpensive sensors to increase imaging performance.

Although synthetic aperture photography has been done with static scenes before, we were the first to capture synthetic aperture videos or to use the technique to look through partial occluders. Our live synthetic aperture system with interactive focal plane adjustment also shows the value of low-level image processing power at the cameras.

The high-speed videography method increases the effective temporal sampling rate of

our system by staggering the trigger times of the cameras. We can compensate for the electronic rolling shutter in many low-end sensors by jittering the camera triggers and re-sampling their output. We have pushed this technique up to 1560fps video using 52 tightly packed, 30fps cameras. The parallel compression in the array lets us stream continuously at this frame rate.

The spatiotemporal view interpolation system I propose simultaneously extends imaging performance along multiple axes–view position and time. It shows that with inexpensive cameras, we can reduce view interpolation of dynamic scenes from estimating three-dimensional structure and motion to determining parallax and two-dimensional image velocities. Much of this gain is due to improved sampling from staggered trigger times, which minimizes image motion between captured views and enables optical-flow based algorithms. The multi-baseline, spatiotemporal optical flow method not only presents a simple framework for synthesizing new virtual views, but also demonstrates that the calibration is adequate for vision algorithms like optical flow, which are sensitive to noise and radiometric camera variations.

We have shown a video capture system for large arrays of inexpensive cameras and applications proving that we can use these cameras for interesting high-performance imaging, computer vision, and graphics applications. Where do we go from here? Our recent experiments with real-time applications using the camera array have produced encouraging results, but performance limits imposed by the architecture are already apparent. We can do low-level image processing at each camera, but image data from multiple cameras can only be combined at the host PC. Thus, the host PCs are the bottleneck for our live synthetic aperture system. The same would be true of any on-the-fly light field compression method that accounts for data redundancy between cameras. Future designs should clearly allow data to flow between cameras. That said, we must develop applications before we can determine the performance needs for a next generation array, and the array as is has already proved to be a valuable tool in that research.

SAP and high-speed videography are but two of the high-x methods enumerated in chapter 2, and it would be interesting to pursue others. As part of the on-going research effort involving the camera array, we are currently exploring the high-resolution approach using cameras with abutting fields of view. We hope to take advantage of the per-camera

processing to individually meter each camera and extend the dynamic range of the mosaic, too. Some global communication to ensure smooth transitions in metering across the array might be necessary.

There still remain several other untapped high-x dimensions: dynamic range, depth of field, spectral resolution, low noise, and so on. One question raised by the high-x applications is, when can a cluster of cameras outperform a single, more expensive camera? For many applications, it will depend on the economics and quality of inexpensive sensors compared to the available performance gain of using many cameras. For example, because the noise reduction from averaging images from n cameras grows only as $sqrt(n)$, if inexpensive cameras have much worse noise performance than the expensive alternative (due to poor optics, more dark current, and so on), they will be unable to affordably close the gap. By contrast, for high-resolution imaging using cameras with abutting fields of view, resolution grows linearly with the number of cameras, while cost most likely grows much faster when increasing the resolution of a single camera. For this reason, I would expect the multiple camera approach to be superior.

For other applications, the consequences of imaging with multiple cameras will fundamentally limit performance regardless of sensor quality or cost. For example, even if our high-speed videography method were not limited by the poor light-gathering ability of inexpensive sensors, we would still have to contend with errors caused by the multiple camera centers of projection. With perfect radiometric camera calibration, we will still see differences between images from adjacent cameras due to specularities and occlusions. These types are artifacts are unavoidable. Optical methods to ensure a common center of projection might be acceptable for some applications, but not for high-speed videography because they reduce the light that reaches each camera.

Attempting to outperform single, high-end cameras will prove fruitful for some applications, but an even richer area to explore is performance gains that are impossible with a single camera. View interpolation itself is one example. Another is the synthetic aperture matting technique I mention in chapter 4. Summing contributions only from pixels in the input images that see through the occluder eliminates the foreground instead of blurring it away and produces images with greater contrast. This nonlinear operation would be impossible with a single large-aperture camera. Surely there exist other opportunities for these

sorts of advances.

The possibilities for improved imaging using arrays of inexpensive cameras are vast, but the tools for exploring them are rare. When I started this project, I did not anticipate that completely reconfiguring an array of one hundred cameras for new applications would someday become a common and undaunting task. I hope this thesis has convinced the reader not only that we can provide the control, capture and calibration capabilities necessary to easily experiment with hundreds of cameras, but also that these experiments will yield rich results.

Appendix A

Spatiotemporal optical flow implementation

In this appendix, I will describe in detail how we solve for spatiotemporal optical flow at virtual view locations. To review, the goal of multibaseline spatiotemporal optical flow is to determine components of image motion due to temporal scene motion and parallax between views of a scene from different positions and times. To make view interpolation simple, we solve for this flow for pixels in the image at the virtual viewing position and time. Our views are parametrized by (x,y,t), where (x,y) is the location in our plane of cameras, and t is the time the image was captured. We use four source views to compute flow because that is the minimum number to enclose a given virtual view in our 3D space-time view coordinates.

We assume that our cameras all lie in a plane and use plane + parallax calibration to determine the displacements, $\mathbf{x}_i$, between the cameras and some reference camera. Note that although we use a reference camera for the displacements (typically a central camera), our algorithm is still truly multi-view, considering all cameras equally, because only the relative displacements between cameras matter. We align all of the images from all cameras to a common reference plane using planar homographies. In the aligned images, for two cameras separated in the camera plane by some relative displacement $\mathbf{x}$, the parallax for a given point at relative depth w is just $w\mathbf{x}$.

We represent temporal scene motion by its two-dimensional projection (u,v) onto the

image plane, similarly to traditional optical flow. Especially for cameras aligned on a plane, estimating motion on the z-axis can be ill-conditioned. Because the camera trigger times are deliberately offset to increase the temporal sampling resolution and ensure that for any virtual view there are several captured views from nearby locations and times, the combined motion due temporal and spatial view changes is minimized.

Multibaseline spatiotemporal optical flow estimates the instantaneous (u,v,w) image flow for each pixel in a virtual view at position and time (x,y,t). It is called multibaseline because it considers multiple source images for each virtual view, and the spatial and temporal distances from the arbitrary virtual view to each of the nearby captured ones are generally different. For each pixel (i,j) in the virtual view, we attempt to solve the following equation with respect to each source image:

$$I_{virtual}(i,j,x,y,t) = I_{source}(i+u\delta t+w\delta x, j+v\delta t+w\delta y, t+\delta t)$$

Optical flow methods traditionally compute a flow error metric by warping one image toward the other based on the computed flow and measuring their difference. Because the virtual image does not exist, we cannot directly compare it to each warped source image. Instead, we measure the accuracy of the computed flow by warping the four nearby space-time views to the virtual view and comparing them to each other.

At this point, we adopt the robust optical flow framework described by Michael Black in [56]. He determines flow in one image with respect to another by minimizing a robust error function with data conservation and spatial smoothness terms. The data conservation term at each pixel is derived from the intensity constancy equation:

$$E_D = \rho_1\left(I_x u + I_y v + I_t, \sigma_1\right)$$

Here, I_x, I_y and I_t are the spatial and temporal image derivatives, and $\rho_1(err,\sigma)$ is some error estimator. $\rho_1(x) = x^2$ would correspond to squared error estimation. The spatial coherence term measures the spatial derivative of the computed flow at each pixel:

$$E_S = \lambda \sum_{n\in\mathbb{G}} \left(\rho_2(u-u_n,\sigma_2) + \rho_2(v-v_n,\sigma_2)\right)$$

where $\mathbb{G}$ are the north, south, east and west neighboring pixels, and u_n and u_v are the computed flow for pixel n in that set. λ sets the relative weight of the smoothness term versus the data term.

Motion discontinuities and occlusions violate assumptions of smoothness and intensity constancy, and create outlier errors that deviate greatly from the Gaussian measurement error assumed by least squares. These outliers have inordinately large influences on squared errors. Black introduces robust error estimators that reduce the effect of these outliers. For his flow implementation, he uses the Lorentzian, whose value $\rho(x,\sigma)$ and derivative $\psi(x,\sigma)$ with respect to a measured error x are:

$$\rho_\sigma(x) = \log\left(1+\frac{1}{2}\left(\frac{x}{\sigma}\right)^2\right)$$

$$\psi_\sigma(x) = \frac{2x}{2\sigma^2+x^2}$$

σ is a scale factor related to the expected values of inliers and outliers.

We too use the Lorentzian estimator. Now, we can formalize our error metric. Although we solve for flow using multiple source images, we compute that flow for pixels in a single virtual image. Thus, the spatial coherence error term E_S is unchanged. Our data coherence term must measure errors between four source images warped to the virtual view according to our three-component flow (u,v,w). To use gradient-based optical flow, we need to compute temporal derivatives between images, so we measure the sum of pairwise robust errors between warped images. Here, we define three new quantities for each source view relative to the virtual view. $\alpha_n = t_n - t_v$ is the temporal offset from the virtual image captured at time t_v to source image I_n captured at time t_n. $(\beta_{nx},\beta_{ny}) = (x_n - x_v, y_n - y_v)$ is the relative displacement in the camera plane from the virtual view to source view I_n. The data conservation error term at each pixel is:

$$E_D = \sum_{m\neq n} \rho_1\Big(I_{x_{m,n}}(u(\alpha_m-\alpha_n)+w(\beta_{mx}-\beta_{nx}))+I_{y_{m,n}}(v(\alpha_m-\alpha_n) + w(\beta_{my}-\beta_{ny}))+I_{t_{m,n}},\sigma_1\Big)$$

Here, $I_{x_{m,n}}$ is the average of the horizontal image spatial derivatives in image I_n and I_m at

the pixel, and likewise for the vertical spatial derivative $I_{y_{m,n}}$. $I_{t_{m,n}}$ is simply $I_m - I_n$ for each pixel.

Now that we have defined robust error functions for multibaseline spatiotemporal optical flow, all that remains is to solve for (u,v,w) at each pixel to minimize the error. We modified Black's publicly available code that calculates flow hierarchically using graduated non-convexity (GNC) and successive over-relaxation (SOR). Hierarchical methods filter and downsample the input images in order to capture large motions using a gradient-based framework. GNC replaces a non-convex error term with a convex one to guarantee a global minimum, then iterates while adjusting the error term steadily towards the desired non-convex one. Successive over-relaxation is an iterative method for the partial differential equations the result from the data consistency and smoothness terms. Readers are referred to [56] more details.

The iterative SOR update equation for minimizing $E = E_D + E_S$ at step $n+1$ has the same form as in Black's work, but we have to update three terms for flow:

$$u^{(n+1)} = u^{(n)} - \omega \frac{1}{T(u)} \frac{\partial E}{\partial u}$$

$$v^{(n+1)} = v^{(n)} - \omega \frac{1}{T(v)} \frac{\partial E}{\partial v}$$

$$w^{(n+1)} = w^{(n)} - \omega \frac{1}{T(w)} \frac{\partial E}{\partial w}$$

where $0 < \omega < 2$ is a parameter used to over correct the estimates for u, v, and w at each step and speed convergence. The first partial derivatives of E with respect to u, v, and w are

$$\frac{\partial E}{\partial u} = \left(\sum_{m \neq n} I_{x_{m,n}} (\alpha_m - \alpha_n) \psi_1(err_{m,n}, \sigma_1) \right) + \lambda \sum_{n \in \mathbb{G}} \psi_2(u - u_n, \sigma_2)$$

$$\frac{\partial E}{\partial v} = \left(\sum_{m \neq n} I_{y_{m,n}} (\alpha_m - \alpha_n) \psi_1(err_{m,n}, \sigma_1) \right) + \lambda \sum_{n \in \mathbb{G}} \psi_2(v - v_n, \sigma_2)$$

$$\frac{\partial E}{\partial w} = \left(\sum_{m \neq n} (I_{x_{m,n}}(\beta_{mx} - \beta_{nx})\psi_1(err_{m,n}) + I_{y_{m,n}}(\beta_{my} - \beta_{ny})\psi_1(err_{m,n})) \right) + \lambda \sum_{\propto \in \mathbb{G}} \psi_2(w - w_n, \sigma_2)$$

where $\mathbb{G}$ as before are north, south, east and west neighbors of each pixel, m and n are from the set {1,2,3,4} of input images, and $err_{m,n}$ is the intensity constancy error:

$$err_{m,n} = I_{x_{m,n}}(u(\alpha_m - \alpha_n) + w(\beta_{mx} - \beta_{nx})) + I_{y_{m,n}}(v(\alpha_m - \alpha_n) + w(\beta_{my} - \beta_{ny})) + I_{t_{m,n}}$$

T(u), T(v), and T(w) are upper bounds on the second partial derivatives of E:

$$T(u) = \left(\sum_{m \neq n} \frac{I_{x_{m,n}}^2 (\alpha_m - \alpha_n)^2}{\sigma_1^2} \right) + \frac{4\lambda}{\sigma_2^2}$$

$$T(v) = \left(\sum_{m \neq n} \frac{I_{y_{m,n}}^2 (\alpha_m - \alpha_n)^2}{\sigma_1^2} \right) + \frac{4\lambda}{\sigma_2^2}$$

$$T(w) = \left(\sum_{m \neq n} \frac{(I_{x_{m,n}}(\beta_{mx} - \beta_{nx}) + I_{y_{m,n}}(\beta_{mx} - \beta_{ny}))^2}{\sigma_1^2} \right) + \frac{4\lambda}{\sigma_2^2}$$

With this, we have all of the pieces to solve for spatiotemporal optical flow using simultaneous over-relaxation.

Bibliography

[1] Y.Y. Schechner and S.K. Nayar. Generalized mosaicing. In *Proceedings of IEEE International Conference on Computer Vision (ICCV)*, Vancouver, Canada, July 2001.

[2] S.Mann and R.W.Picard. Being 'undigital' with digital cameras: Extending dynamic range by combining differently exposed pictures. Technical Report 323, M.I.T. Media Lab Perceptual Computing Section, Boston, Massachusetts, 1994. Also appears, IS&T's 48th annual conference, Cambridge, Massachusetts, May 1995.

[3] Paul E. Debevec and Jitendra Malik. Recovering high dynamic range radiance maps from photographs. In *SIGGRAPH'97*, pages 369–378, August 1997.

[4] R. Szeliski. Image mosaicing for tele-reality applications. In *WACV94*, pages 44–53, 1994.

[5] M. Levoy and P. Hanrahan. Light field rendering. In *Proc. ACM Conference on Computer Graphics (SIGGRAPH'96)*, pages 31–42, New Orleans, USA, August 1996.

[6] A. Isaksen, L. McMillan, and S. Gortler. Dynamically reparametrized light fields. In *Proceedings of ACM SIGGRAPH 2000*, pages 297–306, 2000.

[7] V. Vaish, B. Wilburn, and M. Levoy. Using plane + parallax for calibrating dense camera arrays. In *Proc. IEEE Conference on Computer Vision and Pattern Recognition (CVPR)*, 2004.

[8] N. Joshi. Color calibration for arrays of inexpensive iamge sensors. Technical Report CSTR-2004-02, Stanford University, 2004. http://graphics.stanford.edu/~winograd/reports/2004-02.pdf.

[9] P. Rander, P. Narayanan, and T. Kanade. Virtualized reality: Constructing time-varying virtual worlds from real events. In *Proceedings of IEEE Visualization*, pages 277–283, Phoenix, Arizona, October 1997.

[10] P.J. Nayaranan, P.W. Rander, and T. Kanade. Synchronous capture of image sequences from multiple cameras. Technical Report CMU-RI-TR-95-25, Carnegie Mellon University, December 1995.

[11] T. Kanade, H. Saito, and S. Vedula. The 3d-room: Digitizing time-varying 3d events by synchronized multiple video streams. Technical Report CMU-RI-TR-98-34, Carnegie Mellon University, 1998.

[12] S. Gortler, R. Grzeszczuk, R. Szeliski, and M. Cohen. The lumigraph. In *Proc. ACM Conference on Computer Graphics (SIGGRAPH'96)*, pages 43–54, New Orleans, USA, August 1996.

[13] Stanford spherical gantry. *http://graphics.stanford.edu/projects/gantry/*.

[14] D. Taylor. Virtual camera movement: The way of the future? *American Cinematographer*, 77(9):93–100, September 1996.

[15] J.-C.Yang, M. Everett, C. Buehler, and L. McMillan. A real-time distributed light field camera. In *Eurographics Workshop on Rendering*, pages 1–10, 2002.

[16] C. Zhang and T. Chen. A self-reconfigurable camera array. In *Eurographics Symposium on Rendering*, 2004.

[17] Paul Rademacher and Gary Bishop. Multiple-center-of-projection images. In *SIGGRAPH 1998*, pages 199–206, 1998.

[18] S.E. Chen and L. Williams. View interpolation for image synthesis. In *Proc. ACM Conference on Computer Graphics (SIGGRAPH'93)*, pages 279–288, 1993.

[19] S. M. Seitz and C. R. Dyer. Photorealistic scene reconstruction by voxel coloring. In *Proceedings of the Computer Vision and Pattern Recognition Conference*, pages 1067–1073, 1997.

[20] K. Kutulakos and S. M. Seitz. A theory of shape by space carving. In *Proceedings of IEEE International Conference on Computer Vision (ICCV)*, 1999.

[21] W. Matusik, C. Buehler, R. Raskar, S. Gortler, and L. McMillan. Image-based visual hulls. In *Proceedings of ACM Conference on Computer Graphics (SIGGRAPH-2000)*, pages 369–374, New Orleans, USA, July 2000.

[22] Kostas Daniilidis. The page of omnidirectional vision. *http://www.cis.upenn.edu/kostas/omni.html*.

[23] Shree Nayar. Catadioptric omnidirectional camera. In *IEEE Conference on Computer Vision and Pattern Recognition (CVPR)*, Puerto Rico, June 1997.

[24] M. Irani and S. Peleg. Improving resolution by image registration. *Graphical Models and Image Processing*, 53(3):231–239, May 1991.

[25] Z. Lin and H. Shum. On the fundamental limits of reconstruction-based super-resolution algorithms. In *IEEE Conference on Computer Vision and Pattern Recognition (CVPR)*, 2001.

[26] S. Baker and T. Kanade. Limits on super-resolution and how to break them. In *IEEE Conference on Computer Vision and Pattern Recognition (CVPR)*, June 2000.

[27] A. Finkelstein, C.E. Jacobs, and D.H. Salesin. Multiresolution video. In *Proc. Siggraph 1996*, New Orleans, LA, August 1996.

[28] A. Hertzmann, C.E. Jacobs, B. Curless, and D.H. Salesin. Image analogies. In *Proc. Siggraph 2001*, Los Angeles, CA, August 2001.

[29] H.S. Sawhney, Y. Guo, K. Hanna, R. Kumar, S. Adkins, and S. Zhou. Hybrid stereo camera: An ibr approach for synthesis of very high resolution stereoscopic image sequences. In *Proc. Siggraph 2001*, Los Angeles, CA, August 2001.

[30] J.M. Ogden, E.H. Adelson, J.R. Bergen, and P.J. Burt. Pyramid-based computer graphics. *RCA Engineer*, 30(5), Sept./Oct. 1985.

[31] H. Maruyama, H. Ohtake, T. Hayashida, M. Yamada, K. Kitamura, T. Arai, T.G. Etoh, J. Namiki, T. Yoshida, H. Maruno, Y. Kondo, T. Ozaki, and S. Kanayama. Color video camera of 1,000,000 fps with triple ultrahigh-speed image sensors. In *Proc. 26th International Congress on High-Speed Photography and Photonics*, Alexandria, VA, Sept 2004.

[32] B. Wandell. *Foundations of Vision*. Sinauer Associates, Sunderland, MA, 1995.

[33] B.E. Bayer. Color imaging array, 1976. U.S. Patent 3,971,065.

[34] J.E. Adams. Design of practical color filter array interpolation algorithms for digital cameras. In D. Sinha, editor, *Proceedings of SPIE, Real Time Imaging II*, volume 3028, pages 117–125, 1997.

[35] D.R. Cok. Signal processing method and apparatus for producing interpolated chrominance values in a sampled color image signal, 1987. U.S. Patent 4,642,678.

[36] H. Tian. Analysis of temporal noise in cmos photodiode active pixel sensor. *IEEE Journal of Solid-State Circuits*, 36(1), January 2001.

[37] J. Janesick. Dueling detectors. *OE Magazine*, 2(2):30–33, February 2002.

[38] D. Anderson. *FireWire System Architecture, Second Edition*. Mindshare, Inc, 1999.

[39] J.F. Hamilton and J.E. Adams. Adaptive color plane interpolation in single sensor color electronic camera, 1997. U.S. Patent 5,629,734.

[40] Motorola mcf5206e product summary. http://www.freescale.com/webapp/sps/site/prod_summary.jsp?code=MCF5206E&nodeId=01DFTQ00M9.

[41] R. Hartley and A. Zisserman. *Multiple View Geometry*. Cambridge University Press, 2000.

[42] R.Y. Tsai. A versatile camera calibration technique for high accuracy 3d vision metrology using off–the–shelf tv cameras and lenses. *IEEE Journal of Robotics and Automation*, 3(4):323–344, August 1987.

[43] J. Heikkila and O. Silven. A four-step camera calibration procedure with implicit image correction. In *IEEE Conference on Computer Vision and Pattern Recognition (CVPR)*, 1997.

[44] Zhengyou Zhang. A flexible new technique for camera calibration. *Proc. International Conference on Computer Vision (ICCV'99)*, September 1999.

[45] Vaibhav Vaish. Light field camera calibration. *http://graphics.stanford.edu/ vaibhav/projects/lfca_calib*.

[46] R. Collins. A space sweep approach to true multi image matching. In *IEEE Conference on Computer Vision and Pattern Recognition (CVPR)*, 1996.

[47] R. Szeliski. Shape and appearance modelling from multiple images. In *Workshop on Image Based Rendering and Modelling*, 1998. (http://research.microsoft.com/ szeliski/IBMR98/web/).

[48] E. Shechtman, Y. Caspi, and M. Irani. Increasing space-time resolution in video sequences. In *European Conference on Computer Vision (ECCV)*, May 2002.

[49] R. Kingslake. *Optics in Photography*. SPIE Optical Engineering Press, 1992.

[50] S. Vedula. Image based spatio-temporal modelling and view intepolation of dynamic events. Technical Report CMU-RI-TR-01-37, Carnegie Mellon University, 2001.

[51] H. Nanda and R. Cutler. Practical calibrations for a real-time digital omnidirectional camera. In *IEEE Conference on Computer Vision and Pattern Recognition (CVPR)*, 2001.

[52] Z. Lin and H. Shum. On the number of samples needed in light field rendering with constant-depth assumption. In *IEEE Conference on Computer Vision and Pattern Recognition (CVPR)*, volume 1, pages 588–595, 2000.

[53] J.-X. Chai, X. Tong, S.-C. Chan, and H.-Y. Shum. Plenoptic sampling. *Proc. ACM Conference on Computer Graphics (SIGGRAPH'00)*, New Orleans, USA, pages 307–318, August 2000.

[54] R.I. Carceroni and K.N. Kutulakos. Multi-view scene capture by surfel sampling: From video streams to non-rigid 3d motion, shape & reflectance. In *Int. Conference on Computer Vision*, 1998.

[55] S. Vedula, S. Baker, and T. Kanade. Spatio-temporal view interpolation. In *Eurographics Workshop on Rendering*, pages 1–11, 2002.

[56] M.J. Black and P. Anandan. A framework for the robust estimation of optical flow. In *Proceedings of IEEE International Conference on Computer Vision (ICCV)*, pages 231–236, 1993.

[57] J. Bergen, P. Burt, R. Hingorani, and S. Peleg. A three frame algorithm for estimating two-component image motion. *IEEE Trans. on Pattern Analysis and Machine Intelligence*, 14(9):886–895, 1992.

[58] S.B. Kang, M. Uyttendaele, S. Winder, and R. Szeliski. High dynamic range video. In *ACM SIGGRAPH and ACM Trans. on Graphics*, San Diego, CA, July 2003.